
Citrus-V: Advancing Medical Foundation Models with Unified Medical Image Grounding for Clinical Reasoning

Guoxin Wang[★] Jun Zhao Xinyi Liu Yanbo Liu Xuyang Cao Chao Li
 Zhuoyun Liu Qintian Sun Fangru Zhou Haoqiang Xing Zhenhong Yang

JDH Algo, JD Health International Inc.
<https://jdh-algo.github.io/Citrus-V/>

Abstract

Medical imaging provides critical evidence for clinical diagnosis, treatment planning, and surgical decisions, yet most existing imaging models are narrowly focused and require multiple specialized networks, limiting their generalization. Although large-scale language and multimodal models exhibit strong reasoning and multi-task capabilities, real-world clinical applications demand precise visual grounding, multimodal integration, and chain-of-thought reasoning. We introduce Citrus-V, a multimodal medical foundation model that combines image analysis with textual reasoning. The model integrates detection, segmentation, and multimodal chain-of-thought reasoning, enabling pixel-level lesion localization, structured report generation, and physician-like diagnostic inference in a single framework. We propose a novel multimodal training approach and release a curated open-source data suite covering reasoning, detection, segmentation, and document understanding tasks. Evaluations demonstrate that Citrus-V outperforms existing open-source medical models and expert-level imaging systems across multiple benchmarks, delivering a unified pipeline from visual grounding to clinical reasoning and supporting precise lesion quantification, automated reporting, and reliable second opinions.

1 Introduction

In clinical practice, physicians routinely operate in highly multimodal environments, where medical imaging plays a central role in diagnosis, treatment planning, and surgical decision-making. Accurate interpretation of imaging data is indispensable, as it provides critical evidence that complements textual reports, laboratory results, and patient history. Consequently, any artificial intelligence system intended for clinical deployment must be capable of integrating visual and textual information at a fine-grained, pixel-level resolution while supporting structured reasoning and clinically grounded decision-making.

Existing medical imaging models are largely designed as expert systems specialized for narrow tasks such as lesion detection[1, 2, 3], segmentation[4, 5, 6], classification[3], or report generation[7, 8, 9, 10, 11]. These models often require multiple specialized networks to cover different organs, disease types, or diagnostic tasks, and they rarely generalize effectively across diverse clinical scenarios. While large-scale language and multimodal models[12, 13, 14, 15] have demonstrated remarkable progress, including strong reasoning capabilities[16, 17] and multi-task generalization, applying them to real-world clinical settings remains challenging. Clinical tasks demand not only multimodal

[★]Project Lead.

understanding but also precise visual grounding and integrated chain-of-thought reasoning to interpret complex medical data, support decision-making workflows, and provide reliable second opinions with explainability and clinical fidelity. Existing multimodal medical approaches often fail to provide pixel-level, fine-grained visual insights or to integrate heterogeneous data modalities effectively, which limits their utility in comprehensive diagnostic reasoning.

In our prior work, *Citrus: Leveraging Expert Cognitive Pathways in a Medical Language Model for Advanced Medical Decision Support*[18], we introduced a language-based medical foundation model that incorporated expert-inspired reasoning pathways and demonstrated strong performance across diverse diagnostic tasks. However, Citrus was fundamentally limited to textual modalities and could not directly incorporate medical images, which are indispensable for real-world clinical decision-making.

To meet the demands of modern clinical workflows and build upon our previous work, next-generation medical foundation models[19, 20, 21] must integrate pixel-level understanding[22], structured information extraction[23], and multimodal chain-of-thought reasoning[24]. By combining robust detection and segmentation capabilities, models can achieve precise lesion localization and quantitative analyses, such as tumor measurement and tissue damage assessment. Integrating these visual insights with textual reports enables the generation and interpretation of structured diagnostic information, supporting radiology report writing and providing reliable second clinical opinions. Furthermore, embedding visual evidence into chain-of-thought reasoning allows the model to perform physician-like diagnostic inference, improving both accuracy and interpretability.

In this work, we introduce Citrus-V, an upgraded multimodal medical foundation model built upon the Citrus framework. Citrus-V makes the following key contributions:

1. We construct a unified model that integrates detection, segmentation, and multimodal chain-of-thought reasoning, enabling pixel-level lesion localization, structured report generation, and physician-like diagnostic inference within a single model.
2. To facilitate reproducibility and support the research community, we release Citrus-V along with a curated open-source data suite, including a multimodal chain-of-thought reasoning dataset for report generation, a refined detection and segmentation benchmark with corrected labels, and a medical document understanding benchmark with graded difficulty levels.
3. We further design a novel multimodal training paradigm to accelerate convergence and enhance generalization across diverse imaging and reasoning tasks.

Extensive experiments demonstrate that Citrus-V surpasses existing open-source medical foundation models and expert-level imaging systems across multiple benchmarks, establishing new state-of-the-art performance in both visual and multimodal tasks. By providing a complete pipeline from visual grounding to clinical reasoning, Citrus-V offers critical support for precise lesion quantification, automated radiology reporting, and reliable second opinions, marking a significant step toward general-purpose medical foundation models and the broader adoption of AI in clinical practice.

2 Related Work

This section mainly introduces the work related to the contributions of this paper, which will be elaborated from three aspects below, namely medical multimodal foundation models in Section 2.1, medical image segmentation foundation models in Section 2.2, and chain-of-thought reasoning technology in Section 2.3.

2.1 Medical Multimodal Large Models

Traditional medical AI has long relied on expert-designed systems tailored to specific modalities and diseases. For instance, DAMO Academy’s research on screening for pancreatic and gastric cancers[25, 26] has significantly reduced the cost of detecting major diseases. However, a key limitation is that these approaches require building separate expert models for each imaging modality, disease type, and specific diagnostic task.

Since the introduction of the Transformer architecture [27] and the emergence of ChatGPT[28], large language models(LLM) have been rapidly adapted to the medical domain. The Med-PaLM

series[29, 30] has distinguished itself by advancing medical question answering (QA) through innovative approaches in data curation, evaluation, and prompting strategies, thereby elevating LLM performance toward physician-level competence. Building on open LLaMA architectures, Clinical Camel[31] introduced conversation-based knowledge encoding, transforming dense medical reviews into synthetic conversational data to facilitate domain-specific supervision. Further, IvyGPT[32] explored staged optimization via supervised fine-tuning and reinforcement learning from human feedback(RLHF), achieving notable performance in Chinese medical QA.

However, medical data are inherently multimodal. To accommodate the integration of textual and visual information, recent research has increasingly focused on multimodal foundation models. Early milestones such as LLaVA-Med [33], IRENE [34], and Med-PaLM M [35] demonstrated the feasibility of end-to-end medical vision–language learning. Subsequent studies [36, 37, 38, 39, 40, 41] have scaled both datasets sizes and model capacities, collectively marking a transition from task-specific solutions toward general-purpose medical multimodal large models (MMLMs).

Concurrently with the steady progress in MMLMs, the supported visual modalities have expanded from initially only 2D images to include 3D imaging data. Pioneering efforts like MedBLIP [42] enabled efficient fusion between 3D medical images and text, while RadFM [43] introduced a unified generative architecture supporting multiple tasks, addressing the scarcity of general-purpose foundational models in radiology. More recent work, including M3D [44], Dia-LLaMA [45], and Med-2E3 [46], has further advanced data strategies, task formulations, and model architectures, accelerating the translation of 3D MMLMs into clinical applications.

Despite this progress, two key challenges remain: the scarcity of paired 3D image–report data, and the quadratic complexity of modeling long 3D sequences.

2.2 Medical Image Segmentation Models

Segmentation has been a cornerstone of medical imaging. CNN-based architectures like U-Net[47] and its successors[48, 49] capture multi-scale contextual information through skip connections, in addition, nnU-Net[5], which further demonstrates the power of self-adaptive pipelines, has set benchmarks across diverse datasets. Transformer-based extensions such as UNETR[50] and MedNeXt[51], improving long-range modeling, offer robustness in complex clinical scenarios but remain limited by annotation requirements and adaptability.

The introduction of foundation segmentation models such as SAM[52] and SAM2[53] has motivated medical adaptations like MedSAM[54] and MedSAM2[55, 56]. By leveraging visual or textual prompts, these models provide interactive solutions for delineating medical structures, often requiring minimal user guidance. While highly effective for semi-automatic workflows, such methods depend heavily on prompt quality and lack robustness in large-scale fully automated settings. This motivates research into more tightly coupled multimodal frameworks that can integrate domain priors with general foundation models.

Integrating large language models (LLMs) with vision encoders has opened new paradigms for segmentation. One direction formulates segmentation as text generation, where models such as Florence-2[57] and VisionLLM[58] represent masks through language tokens, though achieving pixel precision remains difficult. Another line introduces task-specific decoders, pioneered by LISA[59], which employs a `<SEG>` token aligned with LLM hidden states. Extensions including LISA++[60], GLAMM[61], SA2VA[62], and X-SAM[63] expand this design to multi-modal and zero-shot segmentation. Finally, unified frameworks such as UFO[64] and Pixel-SAIL[65] aim to integrate detection, segmentation, and pixel understanding within a single transformer architecture, pointing toward scalable and general-purpose solutions.

Extending these ideas to the clinical domain, recent works combine LLMs with medical encoders for multimodal analysis. M3D[66] targets 3D medical segmentation, while MIMO[67] and MedPliB[68] enhance interpretability by coupling segmentation with region-level VQA. UniBioMed[22] further unifies segmentation and diagnostic report generation, offering joint localization and reasoning capabilities. Most approaches adopt parameter-efficient fine-tuning (e.g., LoRA[69]) to preserve language capacity, but this can limit multi-task synergy. By contrast, our method employs full-parameter supervised fine-tuning, encouraging deeper integration of pixel-level segmentation and medical language understanding within a single multimodal large model.

2.3 Chain-of-Thought Reasoning Technology

Large language models have increasingly been found to be prone to hallucination, generating plausible yet nonfactual content. Recently, in-context learning (ICL) techniques empower large language models to demonstrate stepwise reasoning, typically referred to as Chain-of-Thought (CoT) reasoning mechanisms. This approach enables models to break down problems into a series of intermediate steps, where a considerable amount of previous research[70, 71, 72, 73, 74, 75] has concentrated on, improving performance on complex reasoning tasks while further enhancing transparency in the model’s decision-making process.

However, existing studies[70, 76, 73, 77, 78] related to CoT reasoning are largely isolated in the language modality, which has been widely applied to tasks such as mathematical reasoning, commonsense reasoning, and symbolic reasoning. Studies have shown that CoT can not only improve the model’s accuracy on standard benchmark tests (e.g., GSM8K, AQUA-RAT) but also enhance the transparency and interpretability of the model’s reasoning process.

Inspired by the success of models like DeepSeek R1[75] and OpenAI o3[79], researchers are actively exploring how to apply similar reasoning enhancement methods to multimodal large language models (MLLMs). By combining textual and visual information to train models for step-by-step reasoning, Multimodal Chain-of-Thought (MCoT) enables models to better focus on critical regions within visual inputs and establish connections between text and images. Representative examples of previous work include, Multimodal-CoT[80], MVoT[81], Video-of-Thought[82], Audio-CoT[83], PCoT[84], LLaVA-CoT[85], CCoT[86], UV-CoT[87], VisCoT[88]. To some extent, MCoT mitigates hallucinations and facilitates model convergence.

Unlike general-purpose multimodal models, multimodal models in the medical domain place greater emphasis on the interpretability of the CoT reasoning process. To endow models with physician-level or even superior performance in clinical diagnosis, treatment planning, and surgical decision-making, the models must possess sophisticated cognitive reasoning capabilities, specifically the ability to perform iterative reasoning through contextual understanding and self-correction. Models using MCoT can accurately replicate the doctor’s diagnosis and treatment process[24, 89]. They generate diagnostic reports by integrating the image features of lesion areas and medical history texts, which greatly improves the accuracy and efficiency of image diagnosis.

3 Data Curation

In this section, we collect and curate datasets sourced from open-source repositories to ensure diversity in instructions and comprehensiveness in the medical image-caption corpus. Additionally, we include synthesized data specifically designed to improve medical reasoning capabilities and enhance the model’s performance across various downstream task domains.

3.1 Data Collection

3.1.1 Data Source

To enhance the fine-grained visual understanding capabilities of Citrus-V in medical imaging and facilitate curriculum learning for medical instruction tuning, we curated and constructed a curriculum dataset from open-source resources. This curriculum comprises medical image captioning data, medical instruction tuning data, and multimodal data from both medical and general domains, including interpretation tasks involving text, charts, diagrams, and scientific illustrations extracted from journal articles.

Medical Image-caption Data The open-source datasets like PMCOA[90], ROCO[91], contain a large collections of coarse caption of medical images, contributive to align with diversity of medical conceptions, covering different modalities and diseases in biomedical category. Medical image reports are considered as a more comprehensive image-captioning corpus, rigorously curated and vetted by experts, maintained by hospital or health institutions, written by professional radiologists, or taken from informative medical science documentaries. Systematic radiology report formulation, detailed perception and interpretation of medical images are extensively summarized and processed

Table 1: List of Open-Source Dataset Collected. We aggregate public corpora across four categories—medical image–caption, medical multimodal instruction/VQA, medical textual QA and reasoning, and general instruction—to ensure diverse instructions and comprehensive coverage for medical vision–language training. Representative sources include PMCOA/ROCO, LLaVA-Med, MIMIC-CXR(+VQA), VQA-RAD/PMC-VQA, CheXpert Plus, MedQuAD, JMed, and OpenHermes; the full list appears in the table.

Aspect	# Datasets Included
Medical Image-Caption	PMCOA, ROCO, LLaVA-Med, MedPix2.0, CheXpert Plus, MIMIC-CXR, ROCOv2, Quilt-LLaVA, PubMedVision
Medical MM Instruction	VQA-RAD, PMC-VQA, PATH-VQA, SLAKE, MIMIC-CXR-VQA, VQA-Med-2019
	JMED, HealthCareMagic, icliniq, HuatuoGPT2-SFT-GPT4
Medical Textual Data	Citrus-S3, medical-o1-verifiable-problem, Medical-R1-Distill-Data, huatuogpt-o1-for-reasoning, MedReason, MedThoughts, medical-o1-reasoningSFT
	AlpaCare, ApolloCorpus, MedQuAD, MedQA, PMC-LLaMA
General Instruction	LLaVA1.5, PixMo, ALLaVA, OpenHermes-2.5

for intergration. The following dataset were assembled: CheXpert Plus[92], PubMedVision[93], LLaVA-Med[94], ROCOv2[95], IU-Xray[96], MIMIC-CXR[97].

Medical MM Instruction Data Medical image interpreting tasks can be categorized into several distinct types, including anatomical organ identification, imaging features interpretation, lesion localization, diagnosis and symptom inference. The diverse Medical Instruction data comes from open-source dataset including VQA-RAD[98], PathVQA[99], PMC-VQA[100], SLAKE[101], MIMIC-Ext-MIMIC-CXR-VQA[102], VQA-Med-2019[103], supplemented to enrich specific task categories, are curated to enhance the systematicity, comprehensiveness and the reasoning ablility while completing similar task.

Medical Textual Data A substantial amount of medical textual data originates from professional medical examination questions as normal medical instructions including AlpaCare[104], ApolloCorpus[105], MedQuAD[106], [107], PMC-LLaMA[108], anonymized patient-doctor dialogue and medical consultations, including HealthCareMagic[109],icliniq-10k[109], HuatuoGPT2-SFT-GPT4[110], and also records released in our previous work JMED[111], and medical textual reasoning data distilled, including Citrus-S3[111], medical-o1-verifiable-problem[112], Medical-R1-Distill-Data[112], huatuogpt-o1-for-reasoning[112], MedReason[113], MedThoughts-8K[114], medical-o1-reasoningSFT[112], was incorporated and filtered to mitigate potential biases arising from image-dominated multimodal training and enhances the model’s performance on downstream tasks that rely primarily on textual understanding and reasoning.

General Instruction Data In addition, textual and multimodal in general fields are introduced to further improve the performance in locating fine-grained visual details, open-knowledge VQA tasks and additional academic task-oriented datasets. The open-source datasets taken from OKVQA[115], A-OKVQA[116], OCRVQA[117], TextCaps[118], involved and have been improved in the previous work of LLaVA1.5[119]. PixMo[120] contains a diverse array of tasks involving the interpretation and reasoning over diagrams, charts, and illustrations, thereby supporting comprehensive understanding of the charts and tables in the document. OpenHermes2.5[121] and ALLaVa[122] contains high-resolution images with fine-grained captions and complex instructions, utilized to supplement the training corpus with more diverse and complex long-form instructions, thereby enhancing the model’s capabilities.

3.1.2 Data Process

To ensure the quality and utility of the collected comprehensive dataset, we implemented a data processing pipeline, which involves basic filtering methods to remove low-quality or irrelevant

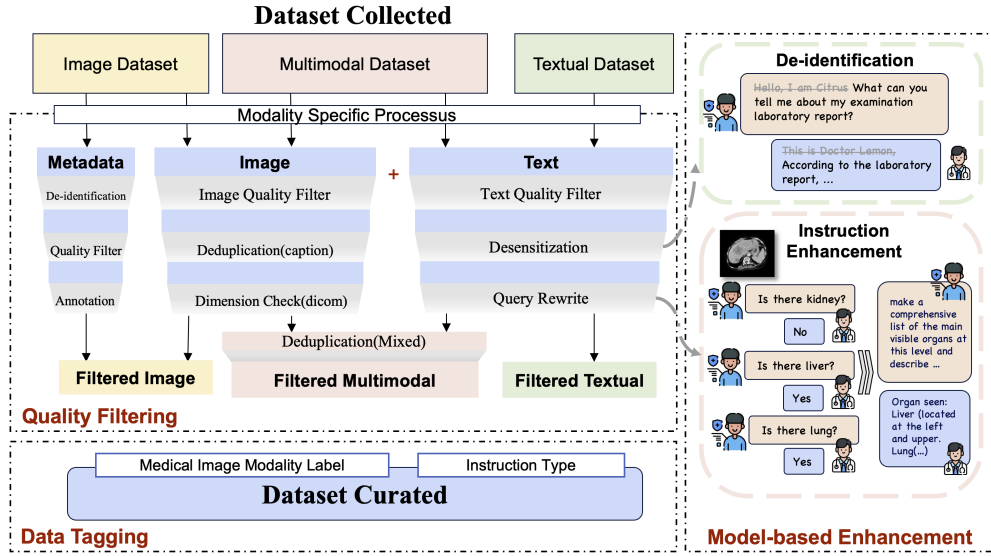


Figure 1: Overview of the Open-source Dataset Filtering and Processing Pipeline. The image and textual data quality is assessed, following with filtering and task-level deduplication, the model-based method are incorporated into the processing pipeline to perform de-identification and instruction enhancement;

samples, and employs model-based enhancement techniques to further refine and enrich the dataset. The following sections details the procedures and criteria adopted. The complete data curation pipeline is illustrated in the Figure 1, which details the procedures and criteria adopted.

Quality Filtering After extensively collecting the aforementioned open-source datasets, rigorous data processing pipeline was applied to both textual(unimodal), image(unimodal) and image-text (multimodal) data. Initially, the quality of images, the metadata included and texts was carefully assessed based on several criteria.

For **image data** in both medical and general domains, 4096 pixels is used as a criterion to filter out low-quality images. For expert-level medical imaging data designated for further synthesis, which are stored in DICOM format with **metadata**, additional criteria—including physical dimension consistency, orientation consistency, and slice-spacing consistency—are applied to ensure data quality. Files exhibiting errors in orientation metadata, specifically in the anterior-posterior, left-right, or superior-inferior directions, are excluded. Furthermore, all personal or private information contained in the metadata is thoroughly removed as part of the data de-identification process.

As for **textual data** sample, low-quality samples were primarily filtered out using methods including regex and token thresholds to remove the sample too short, fewer than 10 or more than 1024 tokens, preventing from the potential no-relevance data, especially for the textual part which concentrates on the image captioning and report generation tasks. Deduplication was also applied to pure text instruction-response pairs to prevent excessive redundancy within the integrated dataset.

In the case of **multimodal** samples, in addition to image and text quality filtering and deduplication, duplication of image-text pairs was identified and removed by combining textual and image hash results, thereby ensuring the uniqueness and overall quality of the dataset.

Model-based Enhancement Model-based methods were applied to portions of the filtered dataset, primarily targeting samples with relatively low instruction and response quality, spotting in the trainset contained in the open-source VQA dataset and for those containing personal privacy information independent from the topic, such as data curated from doctor-patient dialogues or health consultations.

De-identification: Conversational data, originating from real user inputs, can significantly enhance the diversity of the training dataset. However, personal and sensitive information present in these dialogues is often not directly relevant to the underlying medical issues. To ensure the quality and privacy compliance of the training data, for the textual datasets derived from conversational data, to perform de-identification, our strategy involve leveraging large language models (LLMs) to anonymize and rewrite the content, thereby removing personal information unrelated to medical consultation from doctor-patient exchanges, we employed LLMs to systematically remove such information, retaining only content pertinent to medical consultation.

Instruction Enhancement: VQA-type training and evaluation datasets are commonly organized into several categories: short-answer questions, multiple-choice questions, true/false questions, and open-ended questions (distinguished from short-answer questions).

The first issue arises from the limited availability of public medical instruction tuning or VQA data, the scarcity of accompanying labels, and the rarity of expert annotations. As a result, some training sets are constructed by posing multiple questions about the same image, or by including a large number of binary presence/absence queries (e.g., “Is the organ present?”) and various organ identification and localization tasks.

The second issue concerns the nature of responses in most training data: although answers in the training set samples are all provided with minimal word count, the instructions do not explicitly require concise responses. Furthermore, for a given question, homogeneous, similar, or even different perspectives can yield equally valid answers, indicating that while these responses are succinct and correct, they may lack systematicity and comprehensiveness.

For such instruction types, the majority of visual understanding questions may be overly simplistic for models that already possess medical visual capabilities, offering limited benefit for training on complex tasks such as reasoning and visual relationship inference. Therefore, we consider the primary utility of this data to be in improving the model’s ability to follow specific instructions rather than enhancing its reasoning or advanced visual understanding capacity.

Thus, our main object was to enable the model to provide more systematic and comprehensive responses to image-related queries by instruction enhancement. To this end, we performed further processing on datasets featuring brief and simple responses by utilizing a VLM to consolidate multiple questions about a single image into more holistic and focused queries, thereby enhancing the professionalism and depth of image interpretation and relational reasoning across multiple image features in medical imaging in the model’s outputs.

Annotations: For the imaging data, organ and lesion-level annotations are also generated using registration-based methods, which assign labels and ROIs to specified regions within the filtered imaging data. The detailed workflow for this process is described in the following section.

Data Tagging The processed data encompasses a wide range of instruction types, each targeting diverse task categories and imaging modalities within medical images. Data tagging methods were extensively employed to annotate both training and evaluation datasets with corresponding task types. The diversity of instruction formats and the broad coverage of imaging modalities and task categories in the training data contribute to enhancing the model’s performance across a variety of downstream tasks.

To analyze the distribution of different data and clearly illustrate the data distribution and better assess the model’s performance across diverse categories, we systematically annotate all medical data according to imaging modality, task type, and anatomical region. This comprehensive tagging scheme not only provides a transparent overview of the dataset’s composition, but also facilitates a detailed evaluation of the model’s capabilities for each task tag, while highlighting potential biases present within the data. These insights inform targeted refinements of both the dataset and the model. The specific classification scheme is shown in Table 2.

When tagging imaging modalities, a dedicated model is trained to classify images by modality. For task and anatomical region, an LLM is utilized to assign tags. In particular, task tagging requires additional domain expertise. Therefore, a detailed strategy is implemented in which precise definitions and representative examples for each task tag are provided to the LLM to ensure accurate annotation. This curated set of reasoning annotations was then utilized to further enhance the model’s capacity for systematic and robust reasoning as shown in Figure 3.

Table 2: All Labels Employed in the Datasets. Data are tagged by imaging modality, task, and anatomical region to enable stratified analysis. The table lists all labels used for each dimension.

Dimension	Data Tag
Modality	Histopathology, CT, X-Ray, MRI, NIR, Ultrasound, Microscopy, OCT, Dermoscopy, Photograph, Endoscopy, Fundus, Other
Task	Examination Selection, Report Analysis, Prior Comparison, Modality Recognition, Organ Recognition, Image Description, Report Generation, Lesion Localization, Differential Diagnosis, Symptoms Inference, Treatment Generation, Treatment Selection, Treatment Details, Basic, Other
Anatomical Region	Abdomen, Chest, Brain, Neck, Cell, Lower Limb, Upper Limb, Oral Cavity, Eye, Breast, Gastrointestinal Tract, Pelvis, Foot, Joint, Other

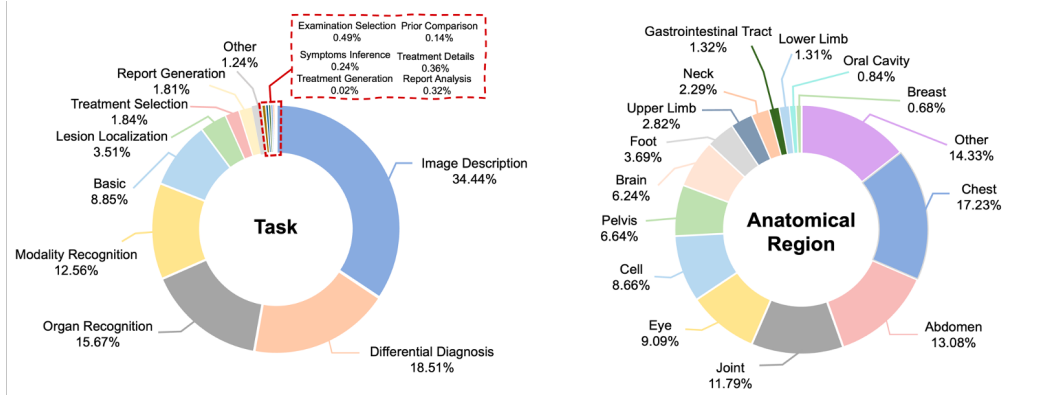


Figure 2: Distribution of Tagged Data. The task tag summarizes the distribution of both text and multimodal test data, while the anatomical region tag summarizes the distribution of multimodal data only.

The modality distribution of data is shown in Section 4.2, while the task and anatomical region distributions are shown in Figure 2. We summarize the distribution of all data in task. Since pure text data do not have corresponding medical images, the statistics for modality and anatomical region are limited to multimodal data only.

3.2 Data Synthesis

3.2.1 Medical Visual Reasoning

In existing multimodal question-answering datasets, the QA format often features relatively short and concise responses, typically limited to multiple-choice, true/false, or short-answer questions, and generally lacking in systematic and comprehensive coverage. While concise question-answer pairs are commonly employed for perception and grounding tasks, the training data also includes QA formats that require more complex reasoning. For such tasks, the absence of explicit reasoning paths may hinder the model’s performance on multimodal tasks that demand intricate inference across heterogeneous information sources.

To address this, we filtered medical VQA queries by response length and query difficulty, and utilized the pipeline illustrated in Figure 3 to synthesize medical VQA reasoning data. This process focuses on specific task types and incorporates challenging VQA items from the training set, ensuring that these complex problems are accompanied by clear analytical pathways leading to correct answers through reasoning.

We employed both a generation model and an answering model to respectively synthesize VQA and VQA reasoning data. Following data annotation, model performance across different data tags was analyzed to highlight specific categories. Representative examples were sampled from the annotated

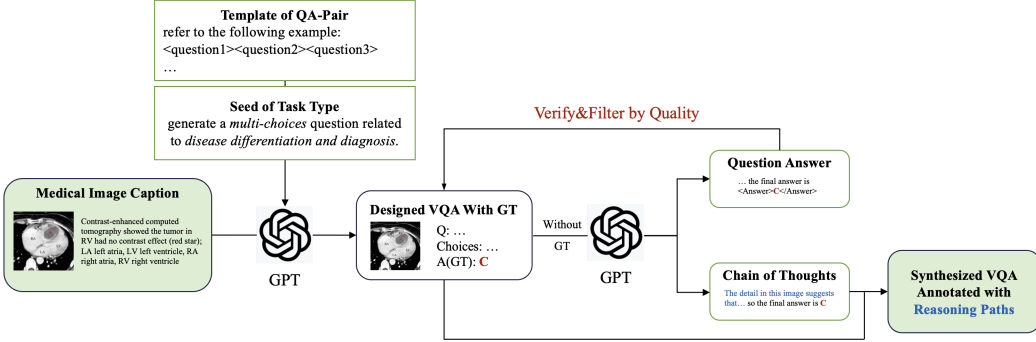


Figure 3: Data Pipeline for Medical Visual Reasoning, different LLMs were employed to (1) generate question-answer pairs with standard answers, tailored according to specific task types, question formats, and image information. (2) annotate the reasoning processes underlying each question-answer pair, thereby verifying the existence of clear and logical reasoning paths, only those reasoning processes that aligned with the designed question answers were retained, ensuring the quality and validity of the annotated data.

data, and specialized prompts were designed to synthesize the required VQA data. Throughout dataset construction, verification procedures ensured that the predefined reasoning paths consistently yielded accurate solutions to complex problems.

3.2.2 Medical Document Understanding

During online or offline consultations, laboratory results, imaging reports, prescriptions, and clinical notes are frequently presented. Public datasets, however, rarely contain real-world text-rich medical document images. To bridge this gap, we curate a corpus of $\sim 2M$ images uploaded by Chinese patients in routine online consultations and build an automated labeling pipeline (Figure 4) using state-of-the-art OCR and vision-language models (VLMs) to extract text, producing QA datasets as training data and a held-out benchmark. Data distribution is in Table 3.

Laboratory Test Reports (LTR) Current VLMs struggle most on laboratory test reports (LTR), which represent a large portion of our corpus (second only to medication-package images) and are clinically critical. The difficulty arises from (i) heterogeneous layouts and dense tabular content; (ii) image quality issues (partial crops, blur, skew/rotation, warping, folds); and (iii) the need for precise numeric comparison against reference intervals to identify abnormalities, which is harder than generic table parsing.

Our pipeline begins with preprocessing to detect orientation and geometric distortion, applying rotation and dewarping to normalize each page. We then perform table parsing with two state-of-the-art VLM parsers that convert each report into a four-column Markdown table (`entry_name`, `result`, `reference`, `unit`); after rule-based normalization, an LLM agreement checker retains only exact or semantic matches. From the normalized tables we derive three types of question-answering (QA) pairs: (i) full parsing, (ii) simple QA that queries a single field, and (iii) complex/abnormality QA that compares `result` against `reference`. For hard-example mining, images are labeled as Easy (Consensus-Before)—consistent full parses obtained without rotation/dewarping—or Hard (Consensus-After)—initially inconsistent parses that become consistent after normalization. Models trained with a higher proportion of Hard samples generalize better to in-the-wild inputs, so our post-training set prioritizes these examples.

General Medical Documents (GMD) Beyond LTR, we extend the pipeline to general medical documents (imaging reports, prescriptions, discharge summaries, etc.). We retain the same core steps—geometry normalization, dual-parser extraction, and LLM agreement checking—but refrain from enforcing a single full-parse schema due to greater format heterogeneity and diverse clinical intents. Instead, we construct document-type-adaptive QA supervision.

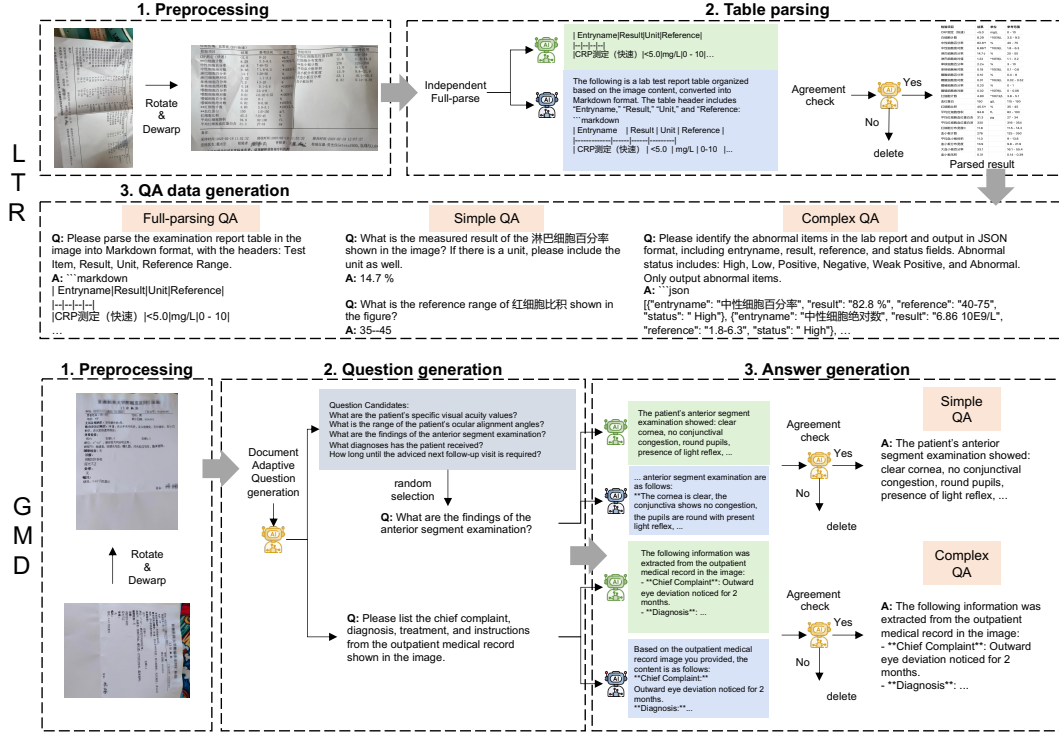


Figure 4: Data Pipeline for Medical Document Understanding. The figure depicts two pipelines—one for Laboratory Test Reports (LTR) and one for General Medical Documents (GMD). Both pipelines apply page-geometry normalization, dual parsing, and LLM-based agreement checking to construct high-quality supervision and mine “hard” cases that require normalization to reach consensus.

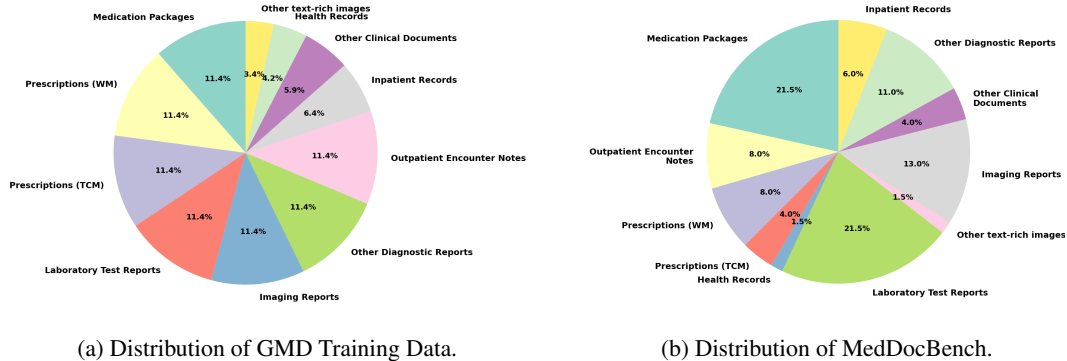


Figure 5: Document Type Distribution of GMD and MedDocBench. The corpus covers a broad set of document types with a long tail of less frequent categories; we downsample overrepresented types to reduce bias while preserving sufficient coverage for rare forms, enabling fairer assessment of cross-type robustness.

We first balance the document-type distribution by downsampling overrepresented categories (Figure 5a) and, as in LTR, apply rotation correction and dewarping. A VLM then generates extraction questions of two kinds—simple (single-fact, sampled from five question candidates) and complex (multi-fact and clinically salient). Each question is answered independently by two state-of-the-art VLMs, and an LLM retains only answers on which they agree. Finally, we perform hard-example mining using the same protocol as LTR (Consensus-Before vs. Consensus-After).

Table 3: Dataset Distribution of Medical Document Understanding across Document Domains, Tasks, and Consensus Buckets. Counts reflect unique QA instances. LTR full parsing targets standardized Markdown tables, while Simple/Complex QA probe single facts and abnormality/compositional reasoning. “Hard” and “Easy” correspond to Consensus-After and Consensus-Before, respectively. The benchmark totals 500 items across tasks.

Domain	Task	Split	# Training Samples	# Benchmark Samples
Laboratory Test Reports	Full-parse	Hard / Easy / All	23,085 / 74,897 / 97,982	100 / - / 100
	Simple QA	Hard / Easy / All	44,786 / 145,998 / 190,784	200 / - / 200
	Complex QA	Hard / Easy / All	23,062 / 74,875 / 97,937	100 / - / 100
General Medical Documents	Simple QA	Hard / Easy / All	83,197 / 21,453 / 104,650	100 / - / 100
	Complex QA	Hard / Easy / All	47,881 / 21,842 / 69,723	100 / - / 100
Total				561,076
				500

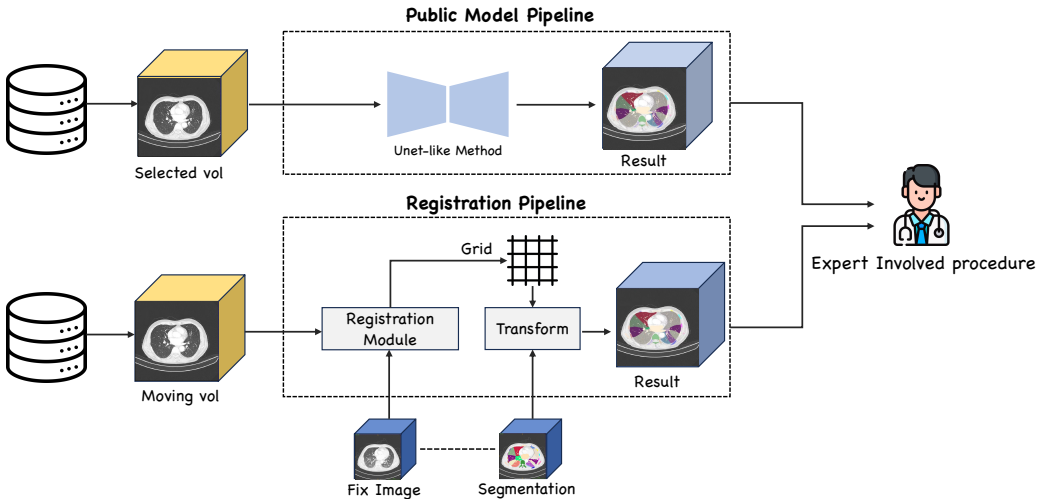


Figure 6: Overview of the Segmentation Data Generation Pipeline. Two branches produce training masks with minimal manual effort: (i) public-model auto-segmentation (e.g., nnU-Net, SegFormer3D) with tiered expert review, and (ii) registration-based label transfer (VoxelMorph with variational refinement) that warps template labels to target scans. Outputs receive light radiologist corrections and are fed back for fine-tuning, yielding scalable, clinically reliable annotations—including rare anatomy—at a fraction of traditional labeling cost.

3.2.3 Medical Image Detection and Segmentation

Labeling medical images at the pixel level is a labor-intensive and costly endeavor, often requiring the expertise of trained radiologists. To address this challenge, we utilize public deep learning models and the ability of registration algorithm.

Public-model pipeline: Off-the-shelf nnU-Net and SegFormer3D checkpoints, pre-trained on large public corpora, generate initial segmentation masks for normal anatomy and common pathologies. A lightweight, tiered review protocol is applied: a junior annotator discards gross failures, a senior radiologist approves or swiftly corrects the remainder, and the refined masks are periodically fed back for model fine-tuning. This human-in-the-loop cycle increases reliable segmentation data by an order of magnitude within days.

Registration pipeline: We employ a VoxelMorph-based registration engine[123] augmented with classical variational refinement to estimate a dense deformation field between a fixed template and a moving CT. The resulting warp propagates the template segmentation to the moving space, yielding anatomy-agnostic, training-ready pseudo-labels for rare malformations, site-specific implants, or congenital variants in seconds Figure 6. After propagation, a radiologist performs light post-labeling corrections, achieving clinical-grade precision while dramatically reducing manual effort.

Impact on manual annotation: By synergising public-model auto-segmentation with registration-driven label transfer, we substitute labor-intensive contouring with rapid machine drafts plus concise

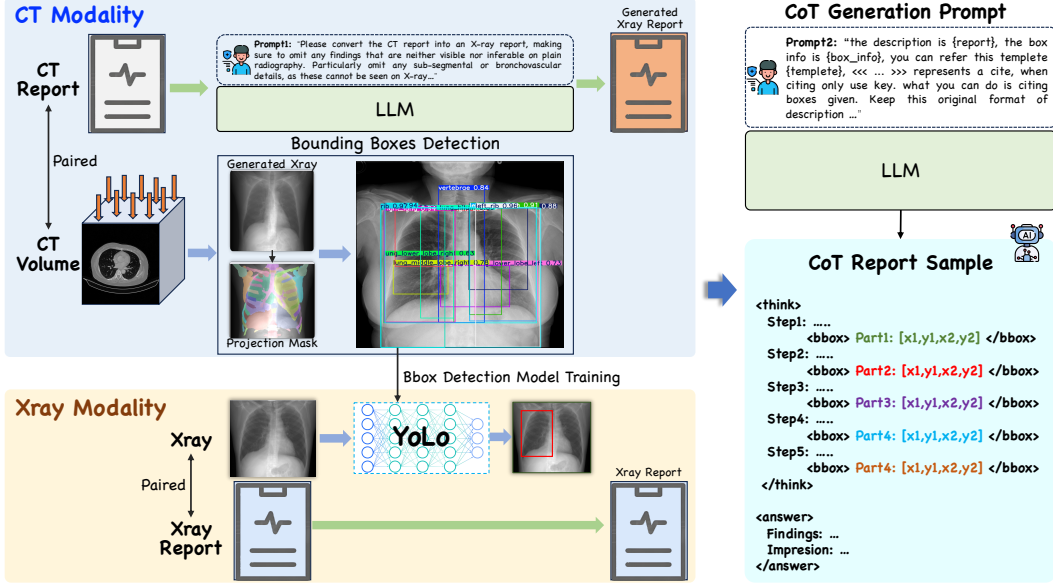


Figure 7: Overview of the CoT-generation Pipeline. CT projection is performed first to synthesize the X-ray image and its bounding boxes; these boxes are directly used to generate the CT-CoT report, while the X-ray-CoT report is produced by a detection model trained with the same projected boxes.

expert review. The former delivers high-quality masks for common structures at scale; the latter extends coverage to uncommon or scanner-specific classes without additional manual slices. Annotators thus focus on light refinement rather than delineation from scratch, slashing pure manual workload ten-fold and compressing dataset expansion from months to days.

3.2.4 Multimodal Chain-of-Thought Reasoning

Chain-of-thought reasoning for medical images remains largely uncharted territory. Our survey shows that public datasets rarely provide step-by-step diagnostic rationales; when CoT-style captions do exist, they seldom reflect the radiologist’s true mental itinerary. Clinicians do not jump from pixels to verdict. Instead, they read the image by focusing on anatomy first: each structure is located, its morphology is measured, and its spatial relationships are evaluated. Only then is a conclusion drawn. In chest radiography, for instance, atelectasis is not declared until the “expansibility” of the two lungs is compared—lung areas, costophrenic angles, and lower border heights are appraised side by side. This deliberate, comparative scrutiny is still missing from today’s CoT annotations.

Motivated by this observation, we introduce a dataset whose diagnostic rationales are explicitly tied to a temporally ordered set of detection boxes, each corresponding to an anatomical structure examined by the radiologist. Rather than curating a fixed list of pathological regions, we adopt a comprehensive approach, modeling the full spectrum of normal, variant, and abnormal anatomical entities. A key impediment to creating such datasets is the challenge of obtaining precise, millimeter-level bounding boxes for anatomical structures in projection radiographs—a task that is both labor-intensive and prone to interobserver variability. To circumvent this, we leverage CT-derived reconstructions, where anatomical boundaries are explicitly defined, and project these labels into the 2D plane to generate accurate, reproducible bounding annotations—without additional manual effort.

CT Projection and Bounding-box Generation: Grounded in the shared physics of CT and X-ray acquisition, we synthesise radiographs by reversible integral projection. Exploiting the Beer–Lambert law, a single 3-D CT volume is cast into line-integral projections at arbitrary angles, yielding digitally reconstructed radiographs (DRRs) that replicate the beam-attenuation, grayscale and contrast behaviour of real radiographs acquired on any X-ray equipment—without the hallucinations or domain-shift risks of AI-driven image synthesis.

Once the CT is projected, the accompanying segmentation mask is rendered at the identical geometry, producing bounding boxes that are spatially exact and free from inter-observer variability. Structures

that are invisible, overlapped or occluded on the DRR remain precisely localised in the transformed mask, giving supervision that is inherently more accurate than any manually drawn annotation.

CT Modality Report Generation: Before the final report is emitted, two preparatory stages are executed (Figure 7). First, Prompt 1 rewrites the original CT report into an X-ray-aware narrative, stripping bronchovascular or sub-segmental details invisible on plain films while retaining clinically observable statements. Second, the draft is aligned with the projected boxes: each sentence is linked to its colour-coded bounding region (green / red / blue), grounding every finding spatially on the DRR. The LLM then produces the CoT report, sequentially citing the responsible boxes and yielding an interpretable, traceable X-ray description.

Xray Modality Report Generation: A detection model is first trained on the projected DRRs and their boxes. After convergence, it is applied to real clinical X-rays to predict bounding boxes, which are fed into the identical CoT pipeline to generate the final X-ray CoT report—closing the loop from 3-D CT to 2-D radiograph reasoning.

CoT Data Generation: Based on the obtained detection boxes and the ground truth radiology reports, we subsequently proceed to generate Chain-of-Thought (CoT) data. GPT-5 was selected for data generation. Specifically, the prompt used for constructing CoT data is shown in the Figure 8a. Compared to previous approaches, our method introduces two major innovations: (1) We incorporate the step of radiologists reviewing the images into the prompt (marked in red color); (2) We prompt the large model to reference the detected regions during its reasoning process. As a result, the CoT training data we construct is illustrated in the Figure 8b. Generally, each sample consists of `<think>` and `<answer>` stages. In the `<think>` stage, the reasoning steps are organized sequentially, for example, ‘rib’ → ‘lung’ → … → ‘heart’, and at each step, the relevant detection regions `<bbox>` that facilitate the model’s reasoning are displayed.

We deliberately pursue both generation routes because these two datasets are intrinsically complementary. On the one hand, CT-derived reports provide a “God’s-eye” view: they capture details that are either invisible or easily confounded on plain radiography. For example, CT can confidently distinguish tuberculosis from bacterial pneumonia, whereas the two often appear nearly identical on X-ray. Training the model on these CT-based descriptions compels it to discover subtle X-ray patterns that correlate with otherwise occult CT findings, thereby curbing hallucination by anchoring the language to a verifiable source. Moreover, the bounding boxes derived from CT projections are essentially noise-free and offer significantly higher spatial fidelity than any box a detection model could produce on real X-rays—an additional layer of supervisory quality.

On the other hand, a curriculum composed solely of synthetic reports would never instill the terse section order, preferred negation style, or curt impression phrasing that human radiologists routinely employ. By blending in authentic X-ray reports, we preserve canonical format, domain-specific vocabulary, and clinical cadence, ensuring that the final CoT output reads like a radiologist’s note rather than a verbose CT abstract forcibly pasted onto a chest film.

3.3 Data Statistics

The training dataset comprises public data and synthesized data generated through a standardized data production pipeline. All data underwent rigorous quality control procedures, including systematic deduplication and comprehensive cleaning. Upon completion of these processes, 16.8M public data and 1.6M synthesized data are curated for model training. Across all data, the total text token length amounts to 3B, and the total number of images exceeds 12.6M. The distribution of the training data is shown in Figure 9.

4 Model Training

4.1 Model Structure

Figure 10 illustrates the overall architecture of our proposed Citrus-V, which consists of three key components: a multimodal large language model (MLLM) for high-level visual–textual reasoning, a segmentation projector that bridges the MLLM and the segmentation model, and a segmentation model for pixel-level delineation. To seamlessly incorporate segmentation capabilities while preserving the reasoning power of the MLLM, we also design a unified segmentation integration strategy,

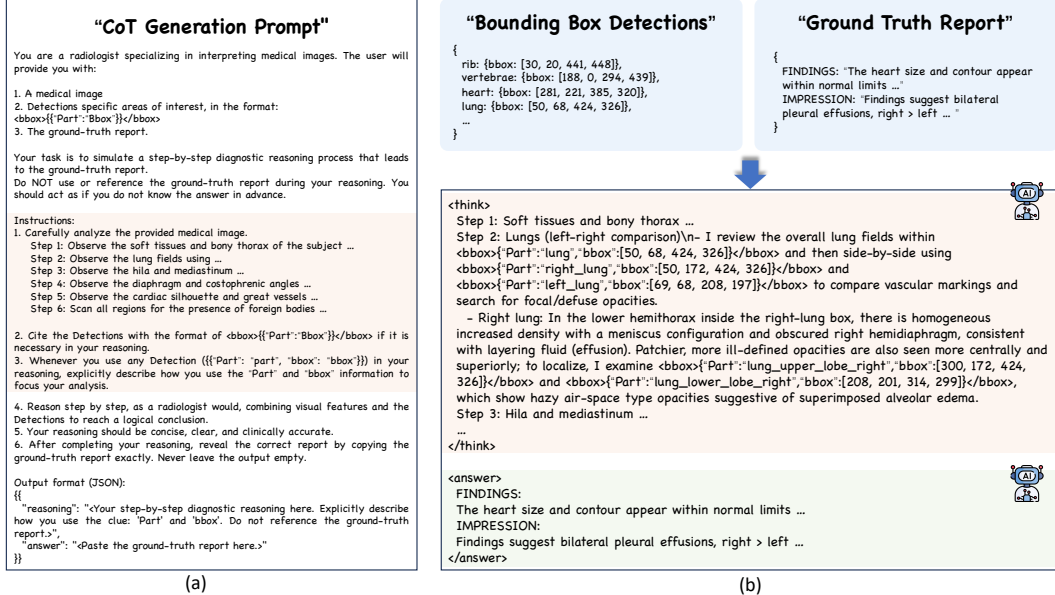


Figure 8: The Construction of chain-of-thought data for Report Generation. By combining the results of Bbox detection with the ground truth reports, we generate CoT reasoning data using the CoT Generation Prompt.

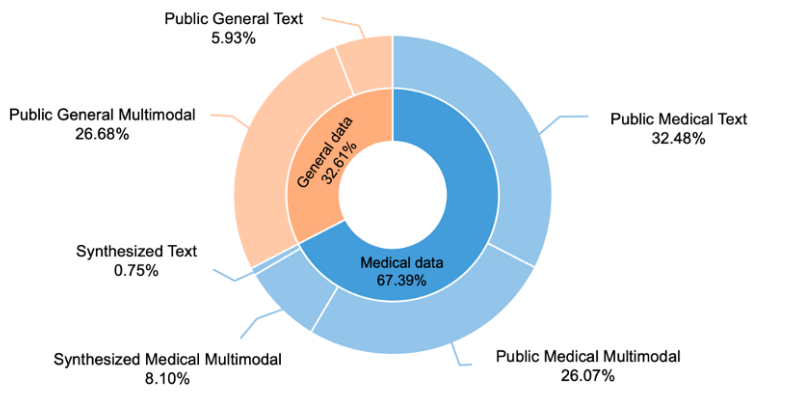


Figure 9: Type Distribution of All Training Data. The corpus combines 16.8M public and 1.6M synthesized samples produced via a standardized pipeline and screened by rigorous QC (systematic deduplication and cleaning). In total it contains >12.6M images and 3B text tokens. The figure shows the proportion of each data type.

which allows the model to perform vision-language understanding and fine-grained segmentation in a coherent, end-to-end framework.

MLLM for Visual-Textual Understanding At the core of Citrus-V lies an MLLM, which serves as the reasoning backbone for tasks such as report generation, VQA, document understanding, and grounding. The MLLM integrates three components: (1) a vision encoder, (2) a text tokenizer, and (3) an LLM. The vision encoder transforms medical images into high-level feature tokens, while the tokenizer converts textual instructions into language tokens. These tokens are jointly fed into the LLM, which performs cross-modal alignment and reasoning, ultimately generating structured or free-text outputs depending on the task.

Segmentation Projector for Latent Prompt Generation While the MLLM effectively interprets and reasons over multimodal inputs, it does not directly produce dense segmentation masks. To enable

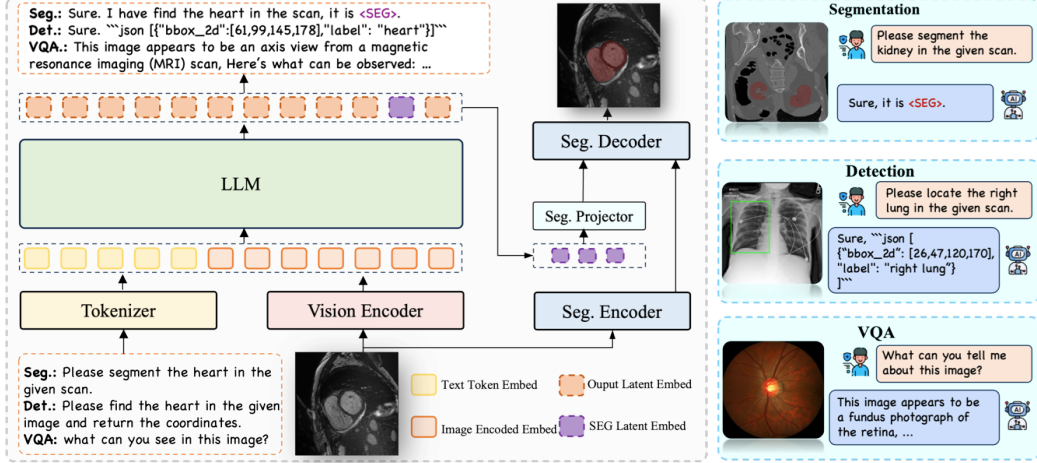


Figure 10: Model Architecture of Citrus-V. The framework consists of three components: (1) an MLLM—including the LLM, tokenizer, and a vision encoder—for high-level visual–textual reasoning such as report generation, VQA, and grounding; (2) a segmentation projector that maps the "[SEG]" token produced by the MLLM into latent segmentation prompts; and (3) a segmentation model that decodes the latent segmentation prompts together with semantic image features into pixel-level masks. Separate image encoders are employed to decouple low-level details for segmentation from high-level semantics for other tasks, ensuring both types of tasks are optimized without semantic conflict.

this capability, Citrus-V introduces a segmentation projector. Specifically, a special token, "[SEG]", is appended to the input sequence, guiding the MLLM to encode the segmentation intent within its hidden states. The projector then maps the hidden representation of the "[SEG]" token into a structured segmentation prompt. This prompt functions as an interface between the MLLM and the downstream segmentation model. By isolating this projection step, Citrus-V decouples language-driven reasoning from pixel-level prediction, ensuring modularity and making the framework extensible to additional vision-centric tasks.

Segmentation Model for Pixel-Level Delineation Similar to existing works, the segmentation model in Citrus-V is inspired by recent prompt-driven segmentation frameworks (e.g., SAM), but is adapted for medical imaging scenarios. It comprises three main components: a vision encoder, a prompt encoder, and a mask decoder. The vision encoder captures multi-scale image features required for accurate delineation of anatomical structures. The prompt encoder processes the projected "[SEG]" prompts from the MLLM, embedding the task-specific instructions into a form compatible with the mask decoder. The mask decoder combines visual features with segmentation prompts to generate pixel-level masks that delineate the target region.

Unlike conventional SAM, which primarily relies on point- or box-based visual prompts, Citrus-V leverages text-derived prompts from the MLLM. This design enables the segmentation model to be flexibly conditioned on natural language queries (e.g., “segment the left atrium” or “highlight tumor boundaries”), allowing for text-guided medical segmentation.

Dual Image Encoder Design By coupling high-level reasoning from the MLLM with fine-grained predictions from the segmentation model, Citrus-V unifies multimodal understanding and pixel-level delineation within a single framework. Citrus-V employs separate image encoders: one designed for high-level semantics (supporting reasoning-oriented tasks such as VQA and grounding), and another specialized for low-level pixel fidelity (supporting segmentation). This separation addresses the conflicting requirements of semantic abstraction versus spatial precision, ensuring that both reasoning and delineation tasks are optimized without compromise.

Unified Segmentation Integration We adopt Qwen2.5-VL[124] as the core multimodal language model, leveraging its strong visual-linguistic reasoning capability. For the segmentation backbone, we integrate SAM2[53], which provides high-quality mask generation. To seamlessly connect these

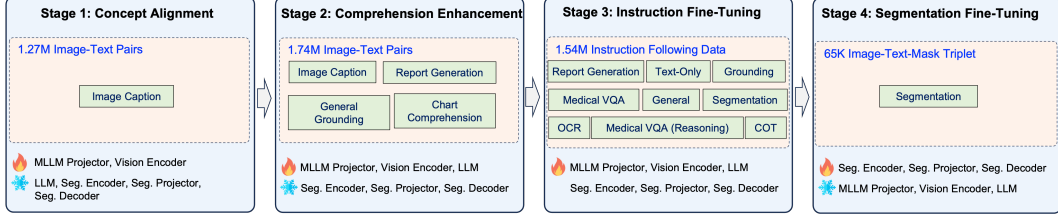


Figure 11: Four Training Stages of the Citrus-V. Consisting of concept alignment, comprehension enhancement, instruction fine-tuning, and segmentation fine-tuning

components, we design a two-layer MLP segmentation projector, mapping MLLM features into the segmentation space.

To preserve the learned knowledge of the strong pretrained MLLM, existing frameworks adopt LoRA[69] to inject segmentation capability into the MLLM while freezing the vision encoder or the whole MLLM[62, 22]. Although LoRA is efficient, it introduces an auxiliary module outside the MLLM, thereby compromising the model’s structural integrity and limiting flexibility during deployment.

To address this, we design a unified segmentation integration strategy that eliminates the need for LoRA while still preserving the original reasoning ability of the MLLM. Concretely, in the first stage, we use large-scale text data to enable the MLLM to learn the usage of the special "[SEG]" token, which encodes segmentation intent within its hidden states. In the second stage, we freeze the entire MLLM and only fine-tune the segmentation projector and the entire segmentation model. This design ensures that the pretrained reasoning and instruction-following capabilities of the MLLM remain intact, while segmentation-specific modules are optimized for precise pixel-level delineation. Through this strategy, Citrus-V achieves a better balance between retaining multimodal generality and enhancing domain-specific segmentation performance, without introducing extra adapters or sacrificing model coherence.

4.2 Training Stages

Figure 11 illustrates the four training stages of Citrus-V, including concept alignment, comprehension enhancement, instruction fine-tuning, and segmentation fine-tuning. The training is designed to progressively adapt the MLLM while mitigating negative transfer between multimodal reasoning and pixel-level segmentation.

Concept Alignment In this stage, most model parameters are frozen, and only the MLLM projector together with the vision encoder are updated. Training primarily relies on image-caption pairs, which establish a stable mapping from visual features into the language space without disrupting the pretrained reasoning ability of the LLM. This step provides a lightweight but essential initialization for subsequent multimodal alignment.

Comprehension Enhancement All MLLM parameters, including the projector, vision encoder, and LLM, are trainable, while the segmentation projector, encoder, and decoder remain frozen. Training incorporates a broader range of tasks, reporting detailed and structured, interpreting of medical image are preserved to establish correlations between visual features, medical concept, radiological findings and imaging diagnostic. Additionally, scientific document comprehension data such as chart, diagram, are taken considering that explication and interpretation of scientific illustrations and graphs is necessary facing with clinical documentation, laboratory reports, diagnostic image annotations and radiographic markers. This stage strengthens the MLLM’s multimodal comprehension capacity, while freezing the segmentation modules prevents premature interference from segmentation supervision.

Instruction Fine-Tuning In the instruction fine-tuning stage, the MLLM is trained on the most diverse instruction-following data, including report generation, text-only instructions, OCR, grounding, medical VQA, reasoning-based chain-of-thought tasks, and segmentation instructions. It is worth noting that our empirical results show that directly combining segmentation loss with other tasks can damage VQA performance significantly. To this end, all MLLM parameters and segmentation

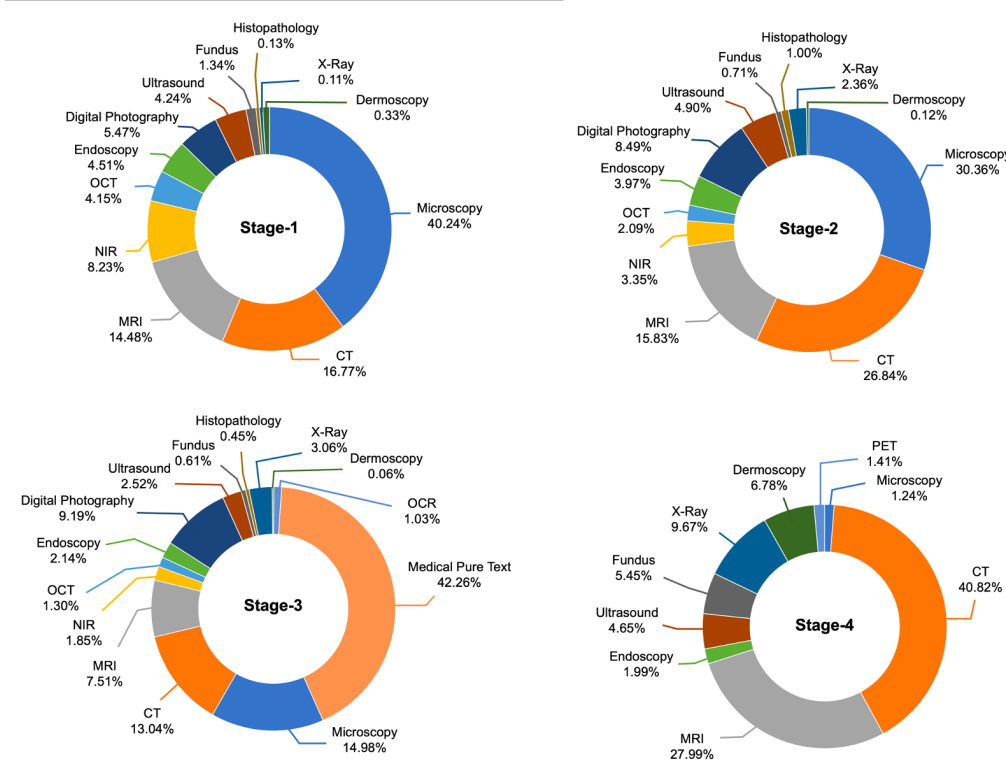


Figure 12: Modality Distribution of Medical Images in Four Training Stages. In total, there are more than 14 different imaging modalities.

modules are updated, while the gradient of segmentation modules is scaled by 0.001 with a hook function. In this way, for segmentation samples, the supervision is restricted to textual outputs containing the special "[SEG]" token, and applying a small mask-level loss. This design allows the MLLM to acquire the discourse patterns needed for segmentation queries and encode segmentation intent into the hidden state of the "[SEG]" token without losing other tasks' performance.

Segmentation Fine-tuning At this stage, all MLLM parameters are frozen, and optimization focuses exclusively on segmentation components, including the segmentation projector, the segmentation encoder, and the segmentation decoder. Unlike prior methods that freeze most of the segmentation backbone, the full SAM2 architecture, including the vision encoder, prompt encoder, and mask decoder, is fine-tuned to adapt effectively to medical imaging. With the MLLM frozen, training is computationally efficient, while full adaptation of SAM2 ensures precise and domain-specific pixel-level segmentation.

The training is conducted in 4 stages with various data. In Stage-1, only public medical multimodal data are used, comprising 1.27M samples. Stage-2 employs both public general and medical multimodal data, with 1.74M samples. For Stage-3, we conduct on a large-scale dataset with 15.4M samples. Stage-4 utilized 65,000 medical multimodal samples for image segmentation training. Within these data, the medical imaging data encompasses over 14 different imaging modalities. The substantial diversity of the training data enhances the robustness and generalization capability of our model. The distributions of medical data modalities within our dataset are illustrated in Figure 12.

Table 4: Model Training Hyperparameters. Training uses DeepSpeed ZeRO-2 with Accelerate, AdamW, and a cosine learning-rate decay. We adopt a staged schedule: stage 1 warms up the visual backbone (ViT) and the visual–text aligner while the LLM is frozen; stages 2–3 jointly fine-tune the LLM with a small LR while continuing to tune ViT and the aligner; stage 4 trains only the segmentation head. A dash (–) indicates the component is frozen in that stage.

Train Phase	LLM LR	ViT LT	Aligner LR	Seg LR	Epochs
stage1	-	2e-6	1e-5	-	1
stage2	1e-5	2e-6	1e-5	-	2
stage3	1e-5	2e-6	1e-5	-	3
stage4	-	-	-	8e-5	10

4.3 Implementation Details

4.3.1 Training Settings

Implementation Details In the first three stages, we mainly adopt the token loss, implemented using the standard cross-entropy loss:

$$\mathcal{L}_{\text{token}} = - \sum_{i=1}^N y_i \log \hat{y}_i, \quad (1)$$

where y_i denotes the ground-truth label and \hat{y}_i denotes the predicted probability of the i -th token.

In the segmentation fine-tuning stage, in addition to the token loss, we incorporate Dice loss and binary cross-entropy (BCE) loss to enhance segmentation accuracy. The Dice loss is defined as:

$$\mathcal{L}_{\text{dice}} = 1 - \frac{2 \sum_{i=1}^N p_i g_i}{\sum_{i=1}^N p_i + \sum_{i=1}^N g_i + \epsilon}, \quad (2)$$

where p_i and g_i denote the predicted probability and ground-truth label of pixel i , respectively, and ϵ is a smoothing term.

The BCE loss is formulated as:

$$\mathcal{L}_{\text{bce}} = - \frac{1}{N} \sum_{i=1}^N [g_i \log p_i + (1 - g_i) \log(1 - p_i)]. \quad (3)$$

The overall segmentation loss is a weighted combination of the three losses:

$$\mathcal{L}_{\text{seg}} = \lambda_1 \mathcal{L}_{\text{token}} + \lambda_2 \mathcal{L}_{\text{dice}} + \lambda_3 \mathcal{L}_{\text{bce}}, \quad (4)$$

where $\lambda_1, \lambda_2, \lambda_3$ are balancing coefficients. In our work, the $\lambda_1, \lambda_2, \lambda_3$ are set 1, 2, and 1, respectively.

Training hyperparameters We use DeepSpeed ZeRO-2 and Accelerate to train the LLM, with AdamW as the optimizer. The hyperparameters for this experiment were set as follows: the learning rate was initialized to 1e-5, with a separate learning rate of 2e-6 for the Vision Transformer component and 1e-5 for the aligner module. A cosine learning rate scheduler was employed. The hyperparameter settings for our model training are shown in Table 4.

4.3.2 Training Framework

We adopt the SWIFT[126] codebase as our training framework and implement several key modifications to accommodate the requirements of our Citrus-V. Following existing works[62, 22], we extend the input template by introducing the "g_pixel_values" key for the segmentation image encoder and the "masks" key for segmentation loss computation. This enables the framework to handle dense segmentation labels alongside standard visual and textual inputs.

In addition, we augment the original Qwen2.5-VL[124] textual output with an additional segmentation mask, encoded in run-length encoding (RLE)[127] to reduce memory consumption and facilitate

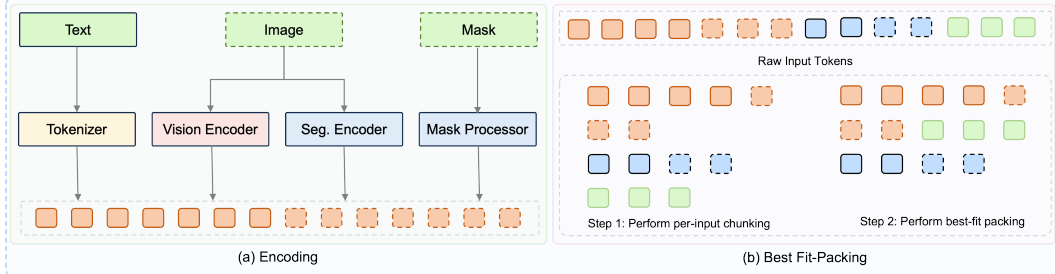


Figure 13: Best-fit Packing Strategy Utilized in Citrus-V. (a) Encoding stage. The input text and image are transformed into tokens using their respective tokenizer or encoder. For segmentation data, an additional mask is processed through the mask encoder. Dashed boxes denote the encoded image or/and mask tokens. (b) Best-fit packing strategy [125]. In this illustrative example, the maximum sequence length is set to 5 tokens. Each box represents a token, with contiguous boxes of the same color indicating one encoded sample. In this example, three samples of lengths 7, 4, and 3 are processed. Step 1: Longer sequences (e.g., the orange one) are split into chunks not exceeding 5 tokens. Step 2: These chunks are then arranged into training sequences so as to minimize the total number of sequences, without further splitting any chunk. In the end, only a single document is truncated, which is required to conform to the maximum sequence length.

efficient storage. This design allows the model to simultaneously generate textual predictions and segmentation outputs, maintaining a unified interface for multimodal tasks.

To enhance training efficiency and support heterogeneous data types, a best-fit packing strategy [125] is employed in Citrus-V, as illustrated in figure 13. Specifically, each input (text, image, or segmentation mask) is first tokenized or encoded into a sequence of tokens. Since different samples vary in length, longer sequences are first segmented into fixed-size chunks that do not exceed the predefined maximum sequence length. These chunks are then packed into training sequences using a best-fit heuristic, which minimizes the total number of sequences while preserving chunk integrity.

We also extend the original data-packing mechanism of SWIFT to enable mixed training of vision-language (e.g., VQA) and segmentation tasks. Within a single packed item, both segmentation and non-segmentation samples can co-exist. To facilitate retrieval of the corresponding segmentation mask and `g_pixel_values` for each “[SEG]” token, the input tensors are augmented with an additional dimension during packing. The resulting packed tensors have the shape $[B, N, C, H, W]$ where B denotes the batch size, N is the number of images or masks in the packed item, and C, H, W correspond to the channel, height, and width, respectively. This design ensures that segmentation data can be efficiently accessed and processed without interfering with non-segmentation samples, thereby improving the overall efficiency and flexibility of mixed-data training, and leading to an approximately $8\times$ improvement in training efficiency under comparable conditions.

5 Experiments

We have deconstructed the underlying capabilities of medical multimodal foundation models into five major categories: **medical visual question answering**, **medical textual question answering**, **medical document understanding**, **medical image report generation**, and **medical image detection and segmentation**. For each capability, we constructed dedicated evaluation datasets, which include both publicly available and proprietary data. Please refer Section 5.1 for detail.

In Section 5.2, We conducted comprehensive comparative experiments on the aforementioned evaluation sets, pitting our model against leading commercial models and open-source medical multimodal models. The results demonstrate the superior performance of our proposed model across various tasks.

Given the critical influence of training data volume, training strategies, and dataset composition on model performance, Section 5.3 performed detailed ablation studies focusing on these dimensions. These experiments are designed to isolate and understand the individual contribution of each factor to the overall model capabilities, providing insights for further optimization.

5.1 Benchmarks

We conducted a detailed evaluation of the model on 16 public and private evaluation datasets. These datasets are organized into 5 categories and listed in detail below. Additionally, we provide a detailed description of the construction process for two of these datasets in the following sections.

Medical Visual Question Answering primarily examines the model’s ability to combine medical-domain visual data (such as CT and MRI images) with related textual questions to automatically generate accurate answers that conform to medical professional logic. The main benchmark datasets for evaluation include: VQA-RAD[98], MedXpertQA[128], SLAKE[101], PATH-VQA[99], and PMC-VQA[100].

Medical Textual Question Answering mainly evaluates the model’s ability to automatically generate accurate answers that comply with medical professional standards for users’ medical-related questions (such as disease diagnosis basis, treatment plans, drug side effects, and explanations of medical concepts) based on text data in the medical field (such as electronic medical records, medical literature, diagnosis and treatment guidelines, and drug instructions). The datasets mainly used for evaluation include: PubMedQA[129], MedMCQA[130], MedQA[131], MedXpertQA[128], CMMLU[132], Medbullets[133], and SuperGPQA[134].

Medical Document Understanding examines the model’s capability to perform in-depth parsing of information such as text, tables, and charts within real-world medical documents (e.g., lab reports, prescription slips) and accurately extract key medical knowledge.

Medical Image Report Generation mainly evaluates the model’s ability to automatically generate structured, clinical-grade radiological diagnosis reports by integrating medical imaging data. The main dataset used for evaluation includes: CheXpert Plus[135].

Medical Image Detection and Segmentation primarily examines the use of large language models to achieve the detection and segmentation of anatomical structures in medical imaging scans. The main benchmark datasets for evaluation include: MeCOVQA-G+, MedSegBench[136] for segmentation task, and MedSAM2[56] for detection task, in which MeCOVQA-G+ is cleaned from MeCOVQA-G[68], MedSegBench covers a wide range of modalities.

5.1.1 MedDocBench

We construct MEDDOCBENCH, a publicly available benchmark for medical document understanding covering routine, patient-uploaded artifacts from online consultations.

Benchmark Statistics. MEDDOCBENCH comprises two tracks: Laboratory Test Reports (LTR) and General Medical Documents (GMD). LTR includes full parsing, simple QA, and complex QA; GMD includes simple QA and complex QA. We release the Hard test sets, which yield a more discriminative and realistic evaluation and better separate top-performing VLMs. See Section 3.2.2 for details on the tracks, splits, and the ground-truth labeling pipeline, and Table 3 and Figure 5b for data distribution.

Evaluation Protocol. LTR: All predictions are canonicalized as a preprocessing step. For full parsing, models output a Markdown table; we perform bipartite matching between predicted and gold entry_names, then assess field-level correctness for entry_name, result, reference, and unit. We report micro Precision/Recall/F1 at the field level and macro-averaged scores at the document (image) level. For complex QA, models return JSON containing the result, reference, and an abnormality label; evaluation follows the same matching procedure with P/R/F1 reporting. For simple QA, we compute exact-match accuracy after canonicalization. In all LTR subtasks, an LLM judge is used as a fallback when rule-based matching failed. GMD: Free-form answers are scored by an LLM judge given the question, the predicted answer, and the gold answer. The judge produces a continuous score $s \in [0, 1]$; we report the mean score. We release the evaluation scripts to support reproducibility.

5.1.2 MeCoVQA-G+

To the best of our knowledge, datasets for training and evaluating text-segmentation alignment in the medical domain are extremely scarce. One of the few publicly available resources is MeCoVQA-G, which was recently introduced alongside the MedPlib paper[135]. MeCoVQA-G is a large-scale, pixel-level VQA subset of the MeCoVQA family, constructed by pairing biomedical images with natural-language questions that explicitly ask the model to segment a given anatomical structure or lesion. Each sample contains a 2-D image slice, a templated question targeting a specific anatomical class, and the corresponding binary segmentation mask as the ground-truth answer. The released split is 100K training pairs and 2,344 test pairs.

However, the formidable challenge of verifying and annotating medical imagery has left the original train/test split riddled with obvious label errors, undermining the scientific rigor of both training and evaluation. To address this, we present MeCoVQA-G+, a thoroughly re-annotated and expanded edition of the corpus. Beyond simply correcting the errors, MeCoVQA-G+ increases both the scale and modality diversity of its predecessor, delivering a more reliable and comprehensive benchmark for medical text-to-segmentation tasks.

We will release the MeCoVQA-G+ test set to establish a new benchmark that specifically addresses the above issues. The set comprises 3,157 carefully curated text-segmentation pairs, in which we have corrected all evident mis-alignments and duplicates. The samples span a wide range of modalities, including X-ray, CT, MRI, ultrasound, and endoscopy. Each image has been meticulously reviewed by a team of medical experts to ensure the accuracy of the segmentation masks.

5.2 Main Results

To conduct a more comprehensive evaluation of model performance, we carried out detailed testing on both commercial models and open-source models using medical datasets. For this purpose, we categorized the models under evaluation into three groups:

Proprietary Models GPT 4.1[137], GPT 5[138], Doubao Seed 1.6[139]

Open-Source Models (<10B) MedGemma 4B[140], Qwen2.5-VL 7B[124], HuatuoGPT-V 7B[141], Lingshu 7B[142]

Open-Source Models (>10B) MedPlib 14B[68], MedGemma 27B[140], Qwen2.5-VL 32B[124], Lingshu 32B[142], HealthGPT 14B[143], HealthGPT 32B[143], HuatuoGPT-V 34B[141]

5.2.1 Medical Textual Question Answering

We conducted a comprehensive evaluation of both commercial and open-source models on open-source medical text question-answering benchmarks to assess their performance in medical text reasoning shown in Table 5. Our findings are as follows. Firstly, despite being trained on a large amount of multimodal data, our Citrus-V 33B model achieved the highest overall average performance, outperforming the second-best model, Lingshu 32B, by 1.44%. Secondly, although MedPlib 14B possesses both image detection/segmentation and medical question-answering capabilities similar to ours, its performance on pure text-based question-answering benchmarks was relatively poor. More specifically, our model achieved the best results on 4 out of 7 test sets, including MedMCQA, CMLLU, Medbullets, and SuperGPQA, and ranked second on the remaining 3 test sets, namely PubMedQA, MedQA, and MedXpertQA.

Among models with fewer than 10 billion parameters, our Citrus-V 8B model still achieves the highest average performance across all evaluation sets, ranking first on 5 out of 7 datasets and outperforming the second-best model, Lingshu 7B, by 0.82%.

5.2.2 Medical Visual Question Answering

Table 6 presents a detailed comparison between Lingshu and a diverse set of both proprietary and open-source MLLMs across seven medical multimodal benchmarks.

Among models with larger than 10B parameters, Citrus-V 33B achieves the highest average score across the evaluation sets, outperforming Lingshu32B (the second-ranked model) by 0.59%. It also

Table 5: Performance of Models on Medical Textual Question Answering Benchmarks. The best results on each benchmark and average accuracy are highlighted in bold, and the scores with underline indicate the second best.

Model	PubMedQA	MedMCQA	MedQA	MedXpertQA	CMMLU	Medbullets	SuperGPQA	Avg.
Proprietary Models								
GPT 4.1	76.00	77.07	87.98	30.82	81.02	73.38	50.6	68.12
GPT 5	78.00	62.99	76.96	40.75	82.93	87.30	49.54	68.35
Doubaod Seed 1.6	76.00	75.06	93.48	30.67	91.67	76.62	55.19	71.24
Open-Source Models (<10B)								
MedGemma 4B	73.00	52.26	55.54	13.1	43.96	42.53	21.52	43.13
Qwen2.5-VL 7B	75.80	53.40	57.50	12.40	68.80	36.69	26.39	47.28
HuatuoGPT-V 7B	73.60	51.95	52.95	10.33	<u>71.12</u>	37.66	22.11	45.67
Lingshu 7B	75.40	56.13	63.39	<u>16.45</u>	69.02	<u>52.92</u>	27.51	51.55
Citrus-V 8B	74.80	<u>55.10</u>	64.89	16.90	71.19	54.22	29.47	52.37
Open-Source Models (>10B)								
MedPlib 14B	49.40	1.63	7.38	0.45	15.53	1.30	0.22	10.84
MedGemma 27B	79.00	63.23	81.15	22.01	60.24	<u>65.58</u>	33.18	57.77
Qwen2.5-VL 32B	68.60	62.71	71.33	15.88	<u>82.60</u>	50.65	38.26	55.72
Lingshu 32B	78.20	<u>65.05</u>	74.94	22.86	82.37	63.31	<u>40.80</u>	<u>61.08</u>
HealthGPT 14B	69.40	63.33	66.93	12.45	55.36	50.00	25.59	49.01
HealthGPT 32B	74.20	64.04	68.89	13.84	69.47	46.43	35.43	53.19
HuatuoGPT-V 34B	71.00	55.08	58.52	12.2	77.64	39.29	28.06	48.83
Citrus-V 33B	78.40	65.62	80.28	<u>22.20</u>	83.27	66.23	41.63	62.52

Table 6: Performance of Models on Medical Visual Question Answering Benchmarks. The best results on each benchmark and average accuracy are highlighted in bold, and the scores with underline indicate the second best.

Model	VQA-RAD	MedXpertQA	SLAKE	PATH-VQA	PMC-VQA	Avg.
Proprietary Models						
GPT 4.1	62.53	43.35	72.54	54.97	38.76	54.43
GPT 5	68.37	51.48	65.82	31.74	36.10	50.70
Doubaod Seed 1.6	33.49	45.75	67.28	47.58	49.94	48.81
Open-Source Models (<10B)						
MedGemma 4B	72.06	22.05	78.32	48.64	48.02	53.82
Qwen2.5-VL 7B	66.30	20.75	67.86	42.30	50.86	49.61
HuatuoGPT-V 7B	67.85	22.30	69.39	44.29	53.84	51.53
Lingshu 7B	<u>68.74</u>	26.90	<u>82.90</u>	<u>60.23</u>	55.77	58.91
Citrus-V 8B	64.30	<u>25.10</u>	84.91	62.00	<u>55.64</u>	<u>58.39</u>
Open-Source Models (>10B)						
MedPlib 14B	45.45	-	38.54	40.02	44.40	-
MedGemma 27B	63.86	33.10	76.17	47.6	45.35	53.22
Qwen2.5-VL 32B	72.28	25.30	76.36	41.58	53.58	53.82
Lingshu 32B	<u>75.39</u>	<u>31.00</u>	<u>87.68</u>	64.76	<u>57.23</u>	<u>63.21</u>
HealthGPT 14B	64.08	24.55	67.43	58.67	56.90	54.33
HealthGPT 32B	64.75	26.40	70.58	62.93	54.93	55.92
HuatuoGPT-V 34B	63.64	22.65	73.02	44.92	56.79	52.20
Citrus-V 33B	77.83	29.15	88.40	<u>63.89</u>	59.74	63.80

establishes state-of-the-art (SOTA) performance on three evaluation sets, *i.e.*, VQA-RAD, SLAKE, and PMC-VQA, while ranking second on the PATH-VQA test set.

Among models with fewer than 10 billion parameters, Citrus-V 8B ranks second in terms of average evaluation metrics, trailing the top model, Lingshu 7B, by 0.52%. Additionally, it achieves state-of-the-art (SOTA) performance on two evaluation sets, namely SLAKE and PATH-VQA.

Although commercial models maintain a clear advantage on medical text QA benchmarks, in medical visual question answering (VQA) scenarios, open-source models fine-tuned on medical multimodal data surpass commercial models in terms of average performance metrics. This is primarily because commercial models excel in text reasoning capabilities. This distinction is evident in that, while commercial models underperform in certain perceptual tasks, such as VQA-RAD, SLAKE, and PATH-VQA, they demonstrate superior results in reasoning-intensive tasks like MedXpertQA.

Table 7: Performance of Models on Medical Document Understanding Benchmarks. The best results on each benchmark and average accuracy are highlighted in bold, and the scores with underline indicate the second best.

Model	Laboratory Test Report			Medical Doc Report		Avg.
	Extract	Simple QA	Complex QA	Simple QA	Complex QA	
Proprietary Models						
GPT 4.1	66.86	71.4	36.66	53.17	55.04	56.63
GPT 5	69.05	<u>78.60</u>	<u>56.78</u>	82.92	64.50	70.37
Doubaol Seed 1.6	80.00	84.72	70.90	81.00	70.92	77.51
Open-Source Models (<10B)						
MedGemma 4B	27.61	19.87	9.56	29.75	25.92	22.54
Qwen2.5-VL 7B	<u>73.23</u>	<u>83.62</u>	<u>31.22</u>	<u>71.92</u>	<u>70.92</u>	<u>66.18</u>
HuatuoGPT-V 7B	23.10	10.26	4.56	25.17	14.21	15.46
Lingshu 7B	60.06	60.48	23.45	53.92	52.28	50.05
Citrus-V 8B	91.21	97.38	84.28	79.75	78.38	86.20
Open-Source Models (>10B)						
MedPlib 14B	-	-	-	-	-	-
MedGemma 27B	26.15	32.97	5.50	29.50	22.21	23.27
Qwen2.5-VL 32B	<u>71.40</u>	<u>83.41</u>	<u>30.54</u>	<u>73.29</u>	<u>73.38</u>	<u>66.40</u>
Lingshu 32B	63.46	73.36	<u>32.38</u>	61.25	62.83	58.66
HealthGPT 14B	22.22	17.90	3.17	24.67	16.00	16.79
HealthGPT 32B	20.95	23.80	2.29	25.08	20.46	18.52
HuatuoGPT-V 34B	22.78	8.52	10.88	22.50	16.12	16.16
Citrus-V 33B	90.01	96.29	87.99	83.08	82.54	87.98

5.2.3 Medical Document Understanding

To evaluate the performance of multimodal language models in medical report interpretation, we conducted assessments in two primary scenarios: laboratory test report question answering (QA) and comprehensive medical document QA. As the entire evaluation dataset is based in Chinese, the commercial model Doubaol Seed 1.6 significantly outperforms the GPT series, with this advantage becoming even more pronounced in complex QA tasks.

As shown in Table 7, among all open-source models with more than 10 billion parameters, Citrus-V 33B demonstrates comprehensive leadership across all evaluation sets, outperforming Qwen2.5-VL 32B (the second-ranked model) by approximately 21.58%. The experimental results also indicate that, although Lingshu 32B performs strongly in medical question-answering scenarios, its effectiveness in medical document understanding drops significantly compared to its base model, with a decrease of about 7.74%. Notably, our model also surpasses the current state-of-the-art commercial models, such as Doubaol Seed 1.6, in terms of average metrics.

Among models with fewer than 10 billion parameters, the Citrus-V 8B model achieves an average evaluation score of 86.2%, outperforming the second-best model, Qwen2.5-VL 7B, by approximately 20.02%, and still maintaining a significant lead over commercial models.

While current medical multimodal language models have achieved promising results in tasks such as medical visual QA, the evaluation shows that all models exhibit varying degrees of performance decline in rich-text image understanding tasks compared to the open-source model Qwen2.5-VL. This suggests that integrating medical image analysis and rich-text image understanding into a unified foundation model remains a significant challenge.

5.2.4 Medical Image Report Generation

Beyond conventional QA tasks, we further evaluate our model on the task of generating radiology reports. CheXpert Plus serves as the benchmark for this part of the experiments. For a fair comparison, we benchmark against a broad set of competitors, categorized into two groups: Proprietary Models and Open-Source Models.

In the Proprietary Models category, well-known systems such as GPT 4.1, GPT 5, and Doubaol Seed1.6 are used as baselines. For open-source models, we differentiate by parameter scale at 10B,

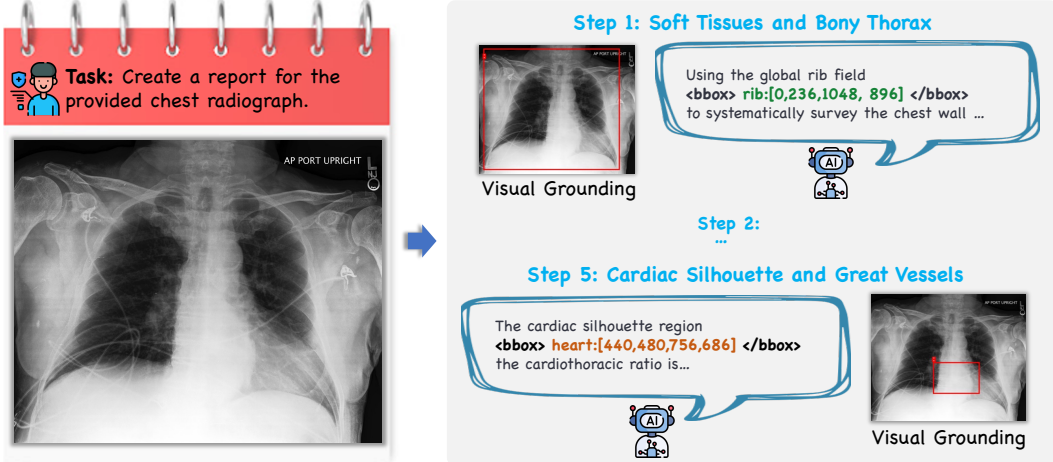


Figure 14: CoT Visualization of Citrus-V on Task of Medical Report Generation. During the reasoning process, Citrus-V leverages visual grounding to localize the corresponding anatomical structures or lesion areas within the medical images, thereby completing a rigorous reasoning process.

yielding two subgroups: Open Source Models (<10B) and Open Source Models (>10B). Specifically, in the <10B group, we include MedGemma 4B, Qwen2.5-VL 7B, HuatuoGPT-V 7B, and Lingshu 7B. In the >10B group, our candidates comprise MedPlib 14B, MedGemma 27B, Qwen2.5-VL 32B, Lingshu 32B, HealthGPT 14B, HealthGPT 32B, and HuatuoGPT-V 34B.

The experimental results are shown in Table 8. We adopt three metrics, ROUGE-L, CIDEr, and RaTE, as our evaluation criteria (ROUGE-L[144], CIDEr[145], and RaTE score(RaTE)[146]). ROUGE-L and CIDEr are used to measure the quality of model-generated reports with respect to reference answers. Following ReXrank and Lingshu, we utilize RaTEScore to measure candidate reports.

Within the Open-Source Models (>10B) group, our Citrus-V 33B achieves the best performance. In CheXpert Plus benchmark, our model achieves a large improvement over the second-place Lingshu 32B. Specifically, ROUGE-L increases by +4.29% (from 25.29 to 29.58), CIDEr by +31.24% (from 77.42 to 108.66), and RaTE by +6.27% (from 46.18 to 52.45).

In the Open-Source Models (<10B) group, our Citrus-V 8B outperforms almost all competitors, achieving an average improvement of +3.82% compared to the second-place MedGemma 4B. Specifically, ROUGE-L increases by +2.93% (from 26.01 to 28.94), and CIDEr increases by +8.71% (from 85.86 to 94.57).

In addition, we present visualization results in Figure 14. As shown by the results, Citrus-V follows the workflow of radiologists when generating reports, exhibiting a rigorous reasoning process. To mitigate the occurrence of hallucinations during reasoning and to further enhance the transparency and interpretability of the model’s thought process, we trained our model to possess grounding capabilities. This enables the model to localize lesions during the reasoning process.

5.2.5 Medical Image Detection and Segmentation

Table 9 primarily presents a performance comparison of multimodal language models on detection and segmentation tasks. We evaluated segmentation performance across eight different image modalities using MedPlib 14B as a baseline, and our Citrus-V 8B model achieved the best segmentation results in all tasks. Since currently only MedPlib 14B and our model are capable of outputting image masks, we have not yet compared these results with other open-source models. Additionally, we assessed our model’s performance on detection tasks, where Citrus-V 8B demonstrated an 23.7% improvement over the base model Qwen2.5-VL 7B.

To determine whether large multimodal language models can match the performance of domain-specific expert models in segmentation tasks, we conducted comparative tests against traditional expert models on several 2D image segmentation datasets, as shown in Table 10. Our Citrus-V 8B outperformed all expert models on 7 out of 8 test subsets and achieved performance metrics

Table 8: Performance of Models on Medical Image Report Generation Benchmarks. The best results on each benchmark are highlighted in bold, and the scores with underline indicate the second best.

Model	CheXpert Plus		
	ROUGE-L	CIDEr	RaTE
Proprietary Models			
GPT 4.1	24.50	78.80	45.50
GPT 5	24.48	86.46	51.26
Doubao Seed 1.6	19.27	61.92	45.49
Open-Source Models (<10B)			
MedGemma 4B	26.01	<u>85.86</u>	51.23
Qwen2.5-VL 7B	22.20	<u>62.00</u>	41.00
HuatuoGPT-V 7B	21.40	65.00	46.58
Lingshu 7B	<u>26.50</u>	79.00	45.40
Citrus-V 8B	28.94	94.57	<u>51.07</u>
Open-Source Models (>10B)			
MedPlib 14B	0.07	0.04	21.05
MedGemma 27B	17.65	48.08	48.73
Qwen2.5-VL 32B	17.45	52.48	46.70
Lingshu 32B	<u>25.29</u>	<u>77.42</u>	46.18
HealthGPT 14B	21.29	68.24	47.82
HealthGPT 32B	12.50	56.38	45.15
HuatuoGPT-V 34B	23.97	66.07	45.51
Citrus-V 33B	29.58	108.66	52.45

Table 9: Performance of Models on Medical Image Detection and Segmentation Benchmarks Compared with MLLMs. The best results on each benchmark are highlighted in bold, and * indicates zero-shot performance. For segmentation task, the evaluation metric is Dice. For detection task, the evaluation is Precision@0.5.

Model	MeCOVQA-G+ _{seg}								MedSAM2 _{det}
	DER	CT	PET	X-RAY	END	MR	US	FP	
MedPlib 14B	79.84	57.58	64.25	8.47*	44.35*	27.38*	34.22*	4.82*	-
Qwen2.5-VL 7B	-	-	-	-	-	-	-	-	20.90
Citrus-V 8B	92.09	64.04	77.93	14.69	92.80	43.07	83.83	74.07	44.60

Table 10: Performance of Models on Medical Image Detection and Segmentation Benchmarks Compared with Specialized Models. The best results on each benchmark are highlighted in bold, and the scores with underline indicate the second best.

Model	MedSegBench								
	Isic2016	Kvasir	Idrib	CovidQUEx	Promise12	MosMedPlus	UltrasoundNerve	Tnbcnuclei	
Unet-MIT	89.10	56.90	5.30	-	-	76.10	-	75.90	
Unet-EfficientNet	<u>90.30</u>	<u>81.20</u>	7.80	74.40	89.20	78.10	<u>78.70</u>	73.80	
Unet-MobileNetV2	89.10	75.40	9.20	74.20	89.60	78.50	77.20	76.20	
Unet-DenseNet121	89.30	79.40	8.90	<u>75.60</u>	90.00	79.10	78.60	<u>78.80</u>	
Unet-ResNet18	87.80	73.90	<u>10.00</u>	74.00	89.50	78.00	78.20	77.90	
Unet-ResNet50	88.70	69.80	9.00	73.40	88.80	<u>79.00</u>	77.60	78.50	
Citrus-V 8B	93.16	90.91	47.10	77.84	90.81	78.17	80.15	82.93	

comparable to expert models on the remaining subset. These results indicate that question answering and segmentation tasks can be effectively integrated into a unified large multimodal language model, with performance that meets or even surpasses that of expert models.

Table 11: Ablation Studies with Different Training Stages on Medical Visual Question Answering Benchmarks. We mainly focus on the impact of the first 2 alignment training stages.

Model	VQA-RAD	MedXpertQA	SLAKE	PATH-VQA	PMC-VQA	Avg.
Qwen2.5-VL 7B	66.30	20.75	67.86	42.30	50.86	49.61
+ stage 3	63.60	19.95	70.77	46.55	55.63	51.30 <small>+1.69</small>
+ stage 1&2&3	67.18	23.45	75.36	47.91	57.71	54.32 <small>+4.71</small>

Table 12: Ablation Studies with Different Training Stages on Medical Images Detection and Segmentation Benchmarks. We mainly focus on the impact of 3rd and 4th training stages.

Model	MeCOVQA-G+ _{seg}								Avg.
	DER	CT	PET	X-RAY	END	MR	US	FP	
Qwen2.5-VL 7B	-	-	-	-	-	-	-	-	-
+ stage 1&2&3	88.22	59.46	69.10	27.20	90.48	36.14	79.72	95.47	66.58
+ stage 1&2&3&4	92.09	64.04	77.93	14.69	92.80	43.07	83.83	74.07	67.82 <small>+1.24</small>

5.3 Ablation Studies

5.3.1 Training Stages

First, we evaluated the impact of the alignment stages on model capabilities using a 7B-scale model, focusing specifically on its performance in medical visual question answering tasks. Detailed results are presented in Table 11. The results show that, after applying the first two alignment stages, the model’s average score across various task metrics increased by 4.71% compared to the baseline model. This demonstrates that fine-tuning the visual encoder during the alignment stage is essential for enhancing the model’s understanding of medical imaging modalities.

Second, we conducted ablation experiments to assess the impact of the fourth alignment stage on segmentation tasks. As shown in Table 12, training with the fourth stage further improved the model’s segmentation accuracy by 1.34%, while maintaining its performance on other understanding tasks. This result confirms the positive effect of fine-tuning during the fourth stage.

5.3.2 Data Types

We conducted detailed experiments to evaluate the impact of textual reasoning data and visual grounding data on model capabilities. Specifically, textual reasoning data was primarily used to assess the model’s performance in question-answering tasks, while visual grounding data was mainly utilized to evaluate the model’s ability to ground anatomical structures during multimodal chain-of-thought reasoning.

Medical Textual Reasoning Data From the experimental results presented in Tables 6 and 5, we observe that commercial models tend to exhibit weaker perceptual capabilities for medical images, as demonstrated on test sets such as VQA-RAD, SLAKE, PATH-VQA, and PMC-VQA. However, they possess exceptionally strong reasoning abilities, as evidenced by their performance on test sets like MedXpertQA and Medbullets. Therefore, this section primarily investigates strategies to enhance the reasoning capabilities of multimodal language models, with a focus on analyzing the impact of two types of data: the medical text reasoning dataset Citrus S3 and the open-source mathematical reasoning dataset AQUA.

In addition to these two datasets, to balance the data distribution across various tasks and improve model performance on downstream tasks, we constructed a balanced dataset of approximately one million samples through random sampling, named CitrusV-1M. This dataset encompasses a diverse array of text-based and multimodal question answering and report generation samples.

During the third stage, we conducted three groups of experiments, sequentially incorporating Citrus-1M, AQUA, and Citrus S3 datasets to evaluate the model’s performance on text and visual question answering tasks involving reasoning. The results of the ablation experiments are presented in Table x. Our observations are as follows. First, after incorporating only Citrus-1M data, the model’s

Table 13: Ablation Studies with Medical Textual Reasoning Data on Medical Reasoning Question Answering Benchmarks.

Model	MedXpertQA		Medbullets		MedQA	PubMedQA	Avg.
	MM	Text	Op4	Op5	-	-	
Qwen2.5-VL 7B	20.75	12.40	47.08	36.69	57.50	75.8	41.70
+ Citrus-1M	24.00	15.10	58.12	48.70	61.74	77.2	47.48 <small>+5.78</small>
+ Citrus-1M + AQUA	25.15	16.16	61.04	51.95	64.10	78.20	49.44 <small>+7.74</small>
+ Citrus-1M + AQUA + Citrus S3	24.8	16.49	59.42	59.74	67.71	76.6	50.79 <small>+9.09</small>

performance on medical reasoning datasets improved by 5.78% over the base model. Second, further addition of AQUA data, although not medically related, provided a positive impact not only on medical text reasoning evaluation sets but also on medical visual reasoning sets such as MedXpertQA-MM, with an average improvement of 1.96%. Third, by further increasing the amount of Citrus S3 data, the model’s average performance on reasoning-related evaluation sets was significantly enhanced, with an improvement of approximately 1.35%. Notably, even when only pure text reasoning data was added, the model showed improvements not only on text reasoning evaluation sets but also on visual reasoning sets such as MedXpertQA-MM.

The ablation experiment results demonstrate that augmenting the model with both medical pure text reasoning datasets and non-medical reasoning datasets can effectively enhance its reasoning ability in the medical question answering domain. This also indirectly illustrates that, despite commercial models not being specifically optimized for the medical domain, their robust general reasoning capabilities enable them to achieve strong performance on medical evaluation sets.

6 Conclusions

In this work, we introduced Citrus-V, a multimodal medical foundation model that unifies pixel-level image grounding with clinical reasoning. By integrating detection, segmentation, and multimodal chain-of-thought reasoning within a single framework, Citrus-V delivers a cohesive pipeline from lesion localization to structured reporting and diagnostic inference. Our novel multimodal training paradigm, combined with the release of a curated open-source data suite, further enhances the development and reproducibility of general-purpose medical foundation models.

Extensive experiments demonstrate that Citrus-V outperforms prior open-source medical foundation models and expert-level imaging systems, setting new benchmarks across both visual and multimodal reasoning tasks. We achieved significant improvements over other open-source models of the same size across five major categories of evaluation sets. Notably, in medical document understanding tasks, our model is able to outperform commercial models. In medical image segmentation tasks, our model’s performance matches or even surpasses that of expert models. For report generation tasks, we introduced multimodal chain-of-thought reasoning to realistically emulate the diagnostic process of physicians, resulting in substantial performance gains on the test sets.

Looking ahead, Citrus-V represents a significant step toward clinically reliable foundation models, offering the potential to support diverse workflows such as precise lesion quantification, automated radiology reporting, and reliable second opinions. By bridging visual grounding with reasoning, Citrus-V paves the way for the next generation of medical AI systems with greater generalizability, interpretability, and clinical utility.

References

- [1] Florin C. Ghesu, Bogdan Georgescu, Sasa Grbic, Andreas Maier, Joachim Hornegger, and Dorin Comaniciu. Towards intelligent robust detection of anatomical structures in incomplete volumetric data. *Medical Image Analysis*, 48:203–213, 2018.
- [2] Jos M. Molina-Casado, Enrique J. Carmona, and Julin Garca-Feijo. Fast detection of the main anatomical structures in digital retinal images based on intra- and inter-structure relational knowledge. *Comput. Methods Prog. Biomed.*, 149(C):55–68, October 2017.
- [3] R. Zwigelaar, S. M. Astley, C. R. M. Boggis, and C. J. Taylor. Linear structures in mammographic images: Detection and classification. *IEEE Transactions on Medical Imaging*, 23(9):1077–1086, 2004.
- [4] Shengzhou Zhong, Wenzhu Wang, Qianjin Feng, Yu Zhang, and Zhenyuan Ning. Cross-view discrepancy-dependency network for volumetric medical image segmentation. *Medical Image Analysis*, 99:103329, 2025.
- [5] Fabian Isensee, Paul F Jaeger, Simon AA Kohl, Jens Petersen, and Klaus H Maier-Hein. nnu-net: a self-configuring method for deep learning-based biomedical image segmentation. *Nature methods*, 18(2):203–211, 2021.
- [6] Shehan Perera, Pouyan Navard, and Alper Yilmaz. Segformer3d: an efficient transformer for 3d medical image segmentation. In *Proceedings of the IEEE/CVF Conference on Computer Vision and Pattern Recognition*, pages 4981–4988, 2024.
- [7] Baoyu Jing, Pengtao Xie, and Eric P Xing. On the automatic generation of medical imaging reports. *arXiv preprint arXiv:1711.08195*, 2018.
- [8] Christy Y Li, Le Lu, Yufeng Yang, George Wu, Arnaud AA Setio, and Ronald M Summers. Hybrid retrieval-generation reinforced agent for medical image report generation. *Advances in neural information processing systems*, 31, 2018.
- [9] Yuan Xue, Yanke Wang, Le Lu, Yufeng Yang, George Wu, Arnaud AA Setio, and Ronald M Summers. Multimodal recurrent model with attention for automated radiology report generation. *Medical image computing and computer - assisted intervention–MICCAI 2018*, pages 450–458, 2018.
- [10] MMA Monshi, J Poon, and V Chung. A survey on automatic generation of medical imaging reports based on deep learning. *Artificial Intelligence in Medicine*, 106:101878, 2020.
- [11] Automated radiology report generation: A review of recent advances. *IEEE Reviews in Biomedical Engineering*, 18:368–387, 2025.
- [12] Weiyun Wang, Zhangwei Gao, Lixin Gu, Hengjun Pu, Long Cui, Xingguang Wei, Zhaoyang Liu, Linglin Jing, Shenglong Ye, Jie Shao, et al. Internvl3. 5: Advancing open-source multimodal models in versatility, reasoning, and efficiency. *arXiv preprint arXiv:2508.18265*, 2025.
- [13] Jinguo Zhu, Weiyun Wang, Zhe Chen, Zhaoyang Liu, Shenglong Ye, Lixin Gu, Hao Tian, Yuchen Duan, Weijie Su, Jie Shao, et al. Internvl3: Exploring advanced training and test-time recipes for open-source multimodal models. *arXiv preprint arXiv:2504.10479*, 2025.
- [14] Kimi Team, Angang Du, Bohong Yin, Bowei Xing, Bowen Qu, Bowen Wang, Cheng Chen, Chenlin Zhang, Chenzhuang Du, Chu Wei, et al. Kimi-vl technical report. *arXiv preprint arXiv:2504.07491*, 2025.
- [15] Wenyi Hong, Weihan Wang, Ming Ding, Wenmeng Yu, Qingsong Lv, Yan Wang, Yean Cheng, Shiyu Huang, Junhui Ji, Zhao Xue, et al. Cogvilm2: Visual language models for image and video understanding. *arXiv preprint arXiv:2408.16500*, 2024.
- [16] Wenyi Hong, Wenmeng Yu, Xiaotao Gu, Guo Wang, Guobing Gan, Haomiao Tang, Jiale Cheng, Ji Qi, Junhui Ji, Lihang Pan, et al. Gilm-4.1 v-thinking: Towards versatile multimodal reasoning with scalable reinforcement learning. *arXiv e-prints*, pages arXiv–2507, 2025.

[17] Zhaochen Su, Peng Xia, Hangyu Guo, Zhenhua Liu, Yan Ma, Xiaoye Qu, Jiaqi Liu, Yanshu Li, Kaide Zeng, Zhengyuan Yang, Linjie Li, Yu Cheng, Heng Ji, Junxian He, and Yi R. Fung. Thinking with images for multimodal reasoning: Foundations, methods, and future frontiers, 2025.

[18] Guoxin Wang, Minyu Gao, Shuai Yang, Ya Zhang, Lizhi He, Liang Huang, Hanlin Xiao, Yexuan Zhang, Wanyue Li, Lu Chen, et al. Citrus: Leveraging expert cognitive pathways in a medical language model for advanced medical decision support. *arXiv preprint arXiv:2502.18274*, 2025.

[19] Jiajia Li, Zhouyu Guan, Jing Wang, Carol Y Cheung, Yingfeng Zheng, Lee-Ling Lim, Cynthia Ciwei Lim, Paisan Ruamviboonsuk, Rajiv Raman, Leonor Corsino, et al. Integrated image-based deep learning and language models for primary diabetes care. *Nature medicine*, 30(10):2886–2896, 2024.

[20] Fei Liu, Hongyu Zhou, Kai Wang, Yunfang Yu, Yuanxu Gao, Zhuo Sun, Sian Liu, Shanshan Sun, Zixing Zou, Zhuomin Li, et al. Metagg: A generative foundation model integrating electronic health records and multimodal imaging for addressing unmet clinical needs. *Cell Reports Medicine*, 6(4), 2025.

[21] Tien Y Wong, Yilan Wu, Bo Qian, Tingyao Li, Yiming Qin, Zhouyu Guan, Tingli Chen, Yali Jia, Ping Zhang, Rajiv Raman, et al. Eyefm: A multi-modal vision-language copilot foundation model for eyecare. *Investigative Ophthalmology & Visual Science*, 66(8):864–864, 2025.

[22] Linshan Wu, Yuxiang Nie, Sunan He, Jiaxin Zhuang, Luyang Luo, Neeraj Mahboobani, Varut Vardhanabuti, Ronald Cheong Kin Chan, Yifan Peng, Pranav Rajpurkar, et al. Unibiomed: A universal foundation model for grounded biomedical image interpretation. *arXiv preprint arXiv:2504.21336*, 2025.

[23] Maurice John O’Kane and Berenice Lopez. Explaining laboratory test results to patients: what the clinician needs to know. *bmj*, 351, 2015.

[24] Zhonghao Yan, Muxi Diao, Yuxuan Yang, Jiayuan Xu, Kaizhou Zhang, Ruoyan Jing, Lele Yang, Yanxi Liu, Kongming Liang, and Zhanyu Ma. Medreasoner: Reinforcement learning drives reasoning grounding from clinical thought to pixel-level precision. *arXiv preprint arXiv:2508.08177*, 2025.

[25] Kai Cao, Yingda Xia, Jiawen Yao, Xu Han, Lukas Lambert, Tingting Zhang, Wei Tang, Gang Jin, Hui Jiang, Xu Fang, et al. Large-scale pancreatic cancer detection via non-contrast ct and deep learning. *Nature medicine*, 29(12):3033–3043, 2023.

[26] Can Hu, Yingda Xia, Zhilin Zheng, Mengxuan Cao, Guoliang Zheng, Shangqi Chen, Jiancheng Sun, Wujie Chen, Qi Zheng, Siwei Pan, et al. Ai-based large-scale screening of gastric cancer from noncontrast ct imaging. *Nature Medicine*, pages 1–9, 2025.

[27] Ashish Vaswani. *Advances in neural information processing systems*. 2017.

[28] Karan Singhal. Toward expert-level medical question answering with large language models. *Nature Medicine*, 31:943–950, 2025.

[29] Karan Singhal. Large language models encode clinical knowledge. *Nature*, 620:172–180, 2023.

[30] Karan Singhal. Toward expert-level medical question answering with large language models. *Nature Medicine*, 31:943–950, 2025.

[31] Augustin Toma, Patrick R Lawler, Jimmy Ba, Rahul G Krishnan, Barry B Rubin, and Bo Wang. Clinical camel: An open expert-level medical language model with dialogue-based knowledge encoding. May 2023.

[32] Rongsheng Wang. Ivygpt: Interactive chinese pathway language model in medical domain. In *CAAI International Conference on Artificial Intelligence*. Springer Nature, Singapore; Singapore, 2023.

[33] Chunyuan Li. Llava-med: Training a large language-and-vision assistant for biomedicine in one day. *Advances in Neural Information Processing Systems*, 36:28541–28564, 2023.

[34] Hong Yu Zhou, Yizhou Yu, Chengdi Wang, Shu Zhang, Yuanxu Gao, Jia Yu Pan, Jun Shao, Guangming Lu, Kang Zhang, and Weimin Li. A transformer-based representation-learning model with unified processing of multimodal input for clinical diagnostics, 2023.

[35] Tao Tu. Towards generalist biomedical AI. *Nejm Ai*, 1(3), 2024.

[36] Stephanie L Hyland, Shruthi Bannur, Kenza Bouzid, Daniel C Castro, Mercy Ranjit, Anton Schwaighofer, Fernando Pérez-García, Valentina Salvatelli, Shaury Srivastav, Anja Thieme, Noel Codella, Matthew P Lungren, Maria Teodora Wetscherek, Ozan Oktay, and Javier Alvarez-Valle. MAIRA-1: A specialised large multimodal model for radiology report generation. November 2023.

[37] Junying Chen, Chi Gui, Ruyi Ouyang, Anningzhe Gao, Shunian Chen, Guiming Hardy Chen, Xidong Wang, Ruifei Zhang, Zhenyang Cai, Ke Ji, Guangjun Yu, Xiang Wan, and Benyou Wang. HuatuoGPT-vision, towards injecting medical visual knowledge into multimodal LLMs at scale. June 2024.

[38] Kai Zhang. A generalist vision-language foundation model for diverse biomedical tasks. *Nature Medicine*, 30:3129–3141, 2024.

[39] Tianbin Li, Yanzhou Su, Wei Li, Bin Fu, Zhe Chen, Ziyan Huang, Guoan Wang, Chenglong Ma, Ying Chen, Ming Hu, Yanjun Li, Pengcheng Chen, Xiaowei Hu, Zhongying Deng, Yuanfeng Ji, Jin Ye, Yu Qiao, and Junjun He. GMAI-VL & GMAI-VL-5.5M: A large Vision-Language model and a comprehensive multimodal dataset towards general medical AI. November 2024.

[40] LASA Team, Weiwen Xu, Hou Pong Chan, Long Li, Mahani Aljunied, Ruifeng Yuan, Jianyu Wang, Chenghao Xiao, Guizhen Chen, Chaoqun Liu, Zhaodonghui Li, Yu Sun, Junao Shen, Chaojun Wang, Jie Tan, Deli Zhao, Tingyang Xu, Hao Zhang, and Yu Rong. Lingshu: A generalist foundation model for unified multimodal medical understanding and reasoning. June 2025.

[41] Andrew Sellergren, Sahar Kazemzadeh, Tiam Jaroensri, Atilla Kiraly, Madeleine Traverse, Timo Kohlberger, Shawn Xu, Fayaz Jamil, Cían Hughes, Charles Lau, Justin Chen, Fereshteh Mahvar, Liron Yatziv, Tiffany Chen, Bram Sterling, Stefanie Anna Baby, Susanna Maria Baby, Jeremy Lai, Samuel Schmidgall, Lu Yang, Kejia Chen, Per Bjornsson, Shashir Reddy, Ryan Brush, Kenneth Philbrick, Mercy Asiedu, Ines Mezerreg, Howard Hu, Howard Yang, Richa Tiwari, Sunny Jansen, Preeti Singh, Yun Liu, Shekoofeh Azizi, Aishwarya Kamath, Johan Ferret, Shreya Pathak, Nino Vieillard, Ramona Merhej, Sarah Perrin, Tatiana Matejovicova, Alexandre Ramé, Morgane Riviere, Louis Rouillard, Thomas Mesnard, Geoffrey Cideron, Jean-Bastien Grill, Sabela Ramos, Edouard Yvinec, Michelle Casbon, Elena Buchatskaya, Jean-Baptiste Alayrac, Dmitry Lepikhin, Vlad Feinberg, Sebastian Borgeaud, Alek Andreev, Cassidy Hardin, Robert Dadashi, Léonard Hussenot, Armand Joulin, Olivier Bachem, Yossi Matias, Katherine Chou, Avinatan Hassidim, Kavi Goel, Clement Farabet, Joelle Barral, Tris Warkentin, Jonathon Shlens, David Fleet, Victor Cotrata, Omar Sanseviero, Gus Martins, Phoebe Kirk, Anand Rao, Shravya Shetty, David F Steiner, Can Kirmizibayrak, Rory Pilgrim, Daniel Golden, and Lin Yang. MedGemma technical report. July 2025.

[42] Qiuwei Chen and Yi Hong. Medblip: Bootstrapping language-image pre-training from 3d medical images and texts. In *Proceedings of the Asian conference on computer vision*. 2024.

[43] Chaoyi Wu. Towards generalist foundation model for radiology by leveraging web-scale 2d&3d medical data. *Nature Communications*, 16, 2025.

[44] Fan Bai, Yuxin Du, Tiejun Huang, Max Q-H Meng, and Bo Zhao. M3D: Advancing 3D medical image analysis with multi-modal large language models. March 2024.

[45] Zhixuan Chen, Luyang Luo, Yequan Bie, and Hao Chen. Dia-LLaMA: Towards large language model-driven CT report generation. March 2024.

[46] Yiming Shi, Xun Zhu, Ying Hu, Chenyi Guo, Miao Li, and Ji Wu. Med-2E3: A 2D-Enhanced 3D medical multimodal large language model. November 2024.

[47] Olaf Ronneberger, Philipp Fischer, and Thomas Brox. U-net: Convolutional networks for biomedical image segmentation. In *International Conference on Medical image computing and computer-assisted intervention*, pages 234–241. Springer, 2015.

[48] Xuyang Cao, Houjin Chen, Yanfeng Li, Yahui Peng, Shu Wang, and Lin Cheng. Uncertainty aware temporal-ensembling model for semi-supervised abus mass segmentation. *IEEE transactions on medical imaging*, 40(1):431–443, 2020.

[49] Zongwei Zhou, Md Mahfuzur Rahman Siddiquee, Nima Tajbakhsh, and Jianming Liang. Unet++: Redesigning skip connections to exploit multiscale features in image segmentation. *IEEE transactions on medical imaging*, 39(6):1856–1867, 2019.

[50] Ali Hatamizadeh, Yucheng Tang, Vishwesh Nath, Dong Yang, Andriy Myronenko, Bennett Landman, Holger R Roth, and Daguang Xu. Unetr: Transformers for 3d medical image segmentation. In *Proceedings of the IEEE/CVF winter conference on applications of computer vision*, pages 574–584, 2022.

[51] Saikat Roy, Gregor Koehler, Constantin Ulrich, Michael Baumgartner, Jens Petersen, Fabian Isensee, Paul F Jaeger, and Klaus H Maier-Hein. Mednext: transformer-driven scaling of convnets for medical image segmentation. In *International Conference on Medical Image Computing and Computer-Assisted Intervention*, pages 405–415. Springer, 2023.

[52] Alexander Kirillov, Eric Mintun, Nikhila Ravi, Hanzi Mao, Chloe Rolland, Laura Gustafson, Tete Xiao, Spencer Whitehead, Alexander C Berg, Wan-Yen Lo, et al. Segment anything. In *Proceedings of the IEEE/CVF international conference on computer vision*, pages 4015–4026, 2023.

[53] Nikhila Ravi, Valentin Gabeur, Yuan-Ting Hu, Ronghang Hu, Chaitanya Ryali, Tengyu Ma, Haitham Khedr, Roman Rädle, Chloe Rolland, Laura Gustafson, et al. Sam 2: Segment anything in images and videos. *arXiv preprint arXiv:2408.00714*, 2024.

[54] Jun Ma, Yuting He, Feifei Li, Lin Han, Chenyu You, and Bo Wang. Segment anything in medical images. *Nature Communications*, 15(1):654, 2024.

[55] Jiayuan Zhu, Abdullah Hamdi, Yunli Qi, Yueming Jin, and Junde Wu. Medical sam 2: Segment medical images as video via segment anything model 2. *arXiv preprint arXiv:2408.00874*, 2024.

[56] Jun Ma, Zongxin Yang, Sumin Kim, Bihui Chen, Mohammed Baharoon, Adibvafa Fallahpour, Reza Asakereh, Hongwei Lyu, and Bo Wang. Medsam2: Segment anything in 3d medical images and videos. *arXiv preprint arXiv:2504.03600*, 2025.

[57] Bin Xiao, Haiping Wu, Weijian Xu, Xiyang Dai, Houdong Hu, Yumao Lu, Michael Zeng, Ce Liu, and Lu Yuan. Florence-2: Advancing a unified representation for a variety of vision tasks. In *Proceedings of the IEEE/CVF Conference on Computer Vision and Pattern Recognition*, pages 4818–4829, 2024.

[58] Wenhui Wang, Zhe Chen, Xiaokang Chen, Jiannan Wu, Xizhou Zhu, Gang Zeng, Ping Luo, Tong Lu, Jie Zhou, Yu Qiao, et al. Visionllm: Large language model is also an open-ended decoder for vision-centric tasks. *Advances in Neural Information Processing Systems*, 36:61501–61513, 2023.

[59] Xin Lai, Zhuotao Tian, Yukang Chen, Yanwei Li, Yuhui Yuan, Shu Liu, and Jiaya Jia. Lisa: Reasoning segmentation via large language model. In *Proceedings of the IEEE/CVF Conference on Computer Vision and Pattern Recognition*, pages 9579–9589, 2024.

[60] Senqiao Yang, Tianyuan Qu, Xin Lai, Zhuotao Tian, Bohao Peng, Shu Liu, and Jiaya Jia. Lisa++: An improved baseline for reasoning segmentation with large language model. *arXiv preprint arXiv:2312.17240*, 2023.

[61] Hanoona Rasheed, Muhammad Maaz, Sahal Shaji, Abdelrahman Shaker, Salman Khan, Hisham Cholakkal, Rao M Anwer, Eric Xing, Ming-Hsuan Yang, and Fahad S Khan. Glamm: Pixel grounding large multimodal model. In *Proceedings of the IEEE/CVF Conference on Computer Vision and Pattern Recognition*, pages 13009–13018, 2024.

[62] Haobo Yuan, Xiangtai Li, Tao Zhang, Zilong Huang, Shilin Xu, Shunping Ji, Yunhai Tong, Lu Qi, Jiashi Feng, and Ming-Hsuan Yang. Sa2va: Marrying sam2 with llava for dense grounded understanding of images and videos. *arXiv preprint arXiv:2501.04001*, 2025.

[63] Hao Wang, Limeng Qiao, Zequn Jie, Zhijian Huang, Chengjian Feng, Qingfang Zheng, Lin Ma, Xiangyuan Lan, and Xiaodan Liang. X-sam: From segment anything to any segmentation. *arXiv preprint arXiv:2508.04655*, 2025.

[64] Hao Tang, Chenwei Xie, Haiyang Wang, Xiaoyi Bao, Tingyu Weng, Pandeng Li, Yun Zheng, and Liwei Wang. Ufo: A unified approach to fine-grained visual perception via open-ended language interface. *arXiv preprint arXiv:2503.01342*, 2025.

[65] Tao Zhang, Xiangtai Li, Zilong Huang, Yanwei Li, Weixian Lei, Xueqing Deng, Shihao Chen, Shunping Ji, and Jiashi Feng. Pixel-sail: Single transformer for pixel-grounded understanding. *arXiv preprint arXiv:2504.10465*, 2025.

[66] Fan Bai, Yuxin Du, Tiejun Huang, Max Q-H Meng, and Bo Zhao. M3d: Advancing 3d medical image analysis with multi-modal large language models. *arXiv preprint arXiv:2404.00578*, 2024.

[67] Yanyuan Chen, Dexuan Xu, Yu Huang, Songkun Zhan, Hanpin Wang, Dongxue Chen, Xueping Wang, Meikang Qiu, and Hang Li. Mimo: A medical vision language model with visual referring multimodal input and pixel grounding multimodal output. In *Proceedings of the Computer Vision and Pattern Recognition Conference*, pages 24732–24741, 2025.

[68] Xiaoshuang Huang, Lingdong Shen, Jia Liu, Fangxin Shang, Hongxiang Li, Haifeng Huang, and Yehui Yang. Towards a multimodal large language model with pixel-level insight for biomedicine. In *Proceedings of the AAAI Conference on Artificial Intelligence*, volume 39, pages 3779–3787, 2025.

[69] Edward J Hu, Yelong Shen, Phillip Wallis, Zeyuan Allen-Zhu, Yuanzhi Li, Shean Wang, Lu Wang, Weizhu Chen, et al. Lora: Low-rank adaptation of large language models. *ICLR*, 1(2):3, 2022.

[70] Jason Wei, Xuezhi Wang, Dale Schuurmans, Maarten Bosma, Fei Xia, Ed Chi, Quoc V Le, Denny Zhou, et al. Chain-of-thought prompting elicits reasoning in large language models. *Advances in neural information processing systems*, 35:24824–24837, 2022.

[71] Takeshi Kojima, Shixiang Shane Gu, Machel Reid, Yutaka Matsuo, and Yusuke Iwasawa. Large language models are zero-shot reasoners. *Advances in neural information processing systems*, 35:22199–22213, 2022.

[72] Zhuosheng Zhang, Aston Zhang, Mu Li, and Alex Smola. Automatic chain of thought prompting in large language models. *arXiv preprint arXiv:2210.03493*, 2022.

[73] Denny Zhou, Nathanael Schärli, Le Hou, Jason Wei, Nathan Scales, Xuezhi Wang, Dale Schuurmans, Claire Cui, Olivier Bousquet, Quoc Le, et al. Least-to-most prompting enables complex reasoning in large language models. *arXiv preprint arXiv:2205.10625*, 2022.

[74] Pan Lu, Liang Qiu, Kai-Wei Chang, Ying Nian Wu, Song-Chun Zhu, Tanmay Rajpurohit, Peter Clark, and Ashwin Kalyan. Dynamic prompt learning via policy gradient for semi-structured mathematical reasoning. *arXiv preprint arXiv:2209.14610*, 2022.

[75] Daya Guo, Dejian Yang, Haowei Zhang, Junxiao Song, Ruoyu Zhang, Runxin Xu, Qihao Zhu, Shirong Ma, Peiyi Wang, Xiao Bi, et al. Deepseek-r1: Incentivizing reasoning capability in llms via reinforcement learning. *arXiv preprint arXiv:2501.12948*, 2025.

[76] Xuezhi Wang, Jason Wei, Dale Schuurmans, Quoc Le, Ed Chi, Sharan Narang, Aakanksha Chowdhery, and Denny Zhou. Self-consistency improves chain of thought reasoning in language models. *arXiv preprint arXiv:2203.11171*, 2022.

[77] Wenhui Chen, Xueguang Ma, Xinyi Wang, and William W Cohen. Program of thoughts prompting: Disentangling computation from reasoning for numerical reasoning tasks. *arXiv preprint arXiv:2211.12588*, 2022.

[78] Namgyu Ho, Laura Schmid, and Se-Young Yun. Large language models are reasoning teachers. *arXiv preprint arXiv:2212.10071*, 2022.

[79] OpenAI. Openai o3. <https://openai.com/index/introducing-o3-and-o4-mini/>, 2025. Accessed 2025-09-20.

[80] Zhuosheng Zhang, Aston Zhang, Mu Li, Hai Zhao, George Karypis, and Alex Smola. Multimodal chain-of-thought reasoning in language models. *arXiv preprint arXiv:2302.00923*, 2023.

[81] Chengzu Li, Wenshan Wu, Huanyu Zhang, Yan Xia, Shaoguang Mao, Li Dong, Ivan Vulić, and Furu Wei. Imagine while reasoning in space: Multimodal visualization-of-thought. *arXiv preprint arXiv:2501.07542*, 2025.

[82] Hao Fei, Shengqiong Wu, Wei Ji, Hanwang Zhang, Meishan Zhang, Mong-Li Lee, and Wynne Hsu. Video-of-thought: Step-by-step video reasoning from perception to cognition. *arXiv preprint arXiv:2501.03230*, 2024.

[83] Ziyang Ma, Zhuo Chen, Yuping Wang, Eng Siong Chng, and Xie Chen. Audio-cot: Exploring chain-of-thought reasoning in large audio language model. *arXiv preprint arXiv:2501.07246*, 2025.

[84] Lei Wang, Yi Hu, Jiabang He, Xing Xu, Ning Liu, Hui Liu, and Heng Tao Shen. T-sciq: Teaching multimodal chain-of-thought reasoning via large language model signals for science question answering. In *Proceedings of the AAAI Conference on Artificial Intelligence*, volume 38, pages 19162–19170, 2024.

[85] Guowei Xu, Peng Jin, Ziang Wu, Hao Li, Yibing Song, Lichao Sun, and Li Yuan. Llava-cot: Let vision language models reason step-by-step. *arXiv preprint arXiv:2411.10440*, 2024.

[86] Chancharik Mitra, Brandon Huang, Trevor Darrell, and Roei Herzig. Compositional chain-of-thought prompting for large multimodal models. In *Proceedings of the IEEE/CVF Conference on Computer Vision and Pattern Recognition*, pages 14420–14431, 2024.

[87] Kesen Zhao, Beier Zhu, Qianru Sun, and Hanwang Zhang. Unsupervised visual chain-of-thought reasoning via preference optimization. *arXiv preprint arXiv:2504.18397*, 2025.

[88] Hao Shao, Shengju Qian, Han Xiao, Guanglu Song, Zhuofan Zong, Letian Wang, Yu Liu, and Hongsheng Li. Visual cot: Advancing multi-modal language models with a comprehensive dataset and benchmark for chain-of-thought reasoning. *Advances in Neural Information Processing Systems*, 37:8612–8642, 2024.

[89] Sunggu Kyung, Jinyoung Seo, Hyunseok Lim, Dongyeong Kim, Hyungbin Park, Jimin Sung, Jihyun Kim, Wooyoung Jo, Yoojin Nam, and Namkug Kim. Medregion-ct: Region-focused multimodal llm for comprehensive 3d ct report generation. *arXiv preprint arXiv:2506.23102*, 2025.

[90] Weixiong Lin, Ziheng Zhao, Xiaoman Zhang, Chaoyi Wu, Ya Zhang, Yanfeng Wang, and Weidi Xie. Pmc-clip: Contrastive language-image pre-training using biomedical documents, 2023.

[91] Obioma Pelka, Sven Koitka, Johannes Rückert, Felix Nensa, and Christoph M. Friedrich. Radiology objects in context (roco): A multimodal image dataset. In Danail Stoyanov, Zeike Taylor, Simone Balocco, Raphael Sznitman, Anne Martel, Lena Maier-Hein, Luc Duong, Guillaume Zahnd, Stefanie Demirci, Shadi Albarqouni, Su-Lin Lee, Stefano Moriconi,

Veronika Cheplygina, Diana Mateus, Emanuele Trucco, Eric Granger, and Pierre Jannin, editors, *Intravascular Imaging and Computer Assisted Stenting and Large-Scale Annotation of Biomedical Data and Expert Label Synthesis*, pages 180–189, Cham, 2018. Springer International Publishing.

[92] Pierre Chambon, Jean-Benoit Delbrouck, Thomas Sounack, Shih-Cheng Huang, Zhihong Chen, Maya Varma, Steven QH Truong, Chu The Chuong, and Curtis P. Langlotz. Chexpert plus: Augmenting a large chest x-ray dataset with text radiology reports, patient demographics and additional image formats. *ArXiv*, abs/2405.19538, 2024.

[93] Junying Chen, Chi Gui, Ruyi Ouyang, Anningzhe Gao, Shunian Chen, Guiming Hardy Chen, Xidong Wang, Ruifei Zhang, Zhenyang Cai, Ke Ji, Guangjun Yu, Xiang Wan, and Benyou Wang. Huatuogpt-vision, towards injecting medical visual knowledge into multimodal llms at scale. *ArXiv*, abs/2406.19280, 2024.

[94] Chunyuan Li, Cliff Wong, Sheng Zhang, Naoto Usuyama, Haotian Liu, Jianwei Yang, Tristan Naumann, Hoifung Poon, and Jianfeng Gao. Llava-med: Training a large language-and-vision assistant for biomedicine in one day. *Advances in Neural Information Processing Systems*, 36:28541–28564, 2023.

[95] Johannes Rückert, Louise Bloch, Raphael Brügel, Ahmad Idrissi-Yaghir, Henning Schäfer, Cynthia S. Schmidt, Sven Koitka, Obioma Pelka, Asma Ben Abacha, Alba G. Seco de Herrera, Henning Müller, Peter A. Horn, Felix Nensa, and Christoph M. Friedrich. Rocov2: Radiology objects in context version 2, an updated multimodal image dataset. *Scientific Data*, 11(1):688, 2024.

[96] Dina Demner-Fushman, Marc D Kohli, Marc B Rosenman, Sonya E Shooshan, Laritza Rodriguez, Sameer Antani, George R Thoma, and Clement J McDonald. Preparing a collection of radiology examinations for distribution and retrieval. *Journal of the American Medical Informatics Association*, 23(2):304–310, 2016.

[97] Alistair E. W. Johnson, Tom J. Pollard, Seth J. Berkowitz, Nathaniel R. Greenbaum, Matthew P. Lungren, Chih-ying Deng, Roger G. Mark, and Steven Horng. Mimic-cxr, a de-identified publicly available database of chest radiographs with free-text reports. *Scientific data*, 6(1):1–10, 2019.

[98] Jason J Lau, Soumya Gayen, Asma Ben Abacha, and Dina Demner-Fushman. A dataset of clinically generated visual questions and answers about radiology images. *Scientific data*, 5(1):1–10, 2018.

[99] Usman Naseem, Matloob Khushi, and Jinman Kim. Vision-language transformer for interpretable pathology visual question answering. *IEEE journal of biomedical and health informatics*, 27(4):1681–1690, 2022.

[100] Xiaoman Zhang, Chaoyi Wu, Ziheng Zhao, Weixiong Lin, Ya Zhang, Yanfeng Wang, and Weidi Xie. Pmc-vqa: Visual instruction tuning for medical visual question answering. *arXiv preprint arXiv:2305.10415*, 2023.

[101] Bo Liu, Li-Ming Zhan, Li Xu, Lin Ma, Yan Yang, and Xiao-Ming Wu. Slake: A semantically-labeled knowledge-enhanced dataset for medical visual question answering. In *2021 IEEE 18th international symposium on biomedical imaging (ISBI)*, pages 1650–1654. IEEE, 2021.

[102] Seongsu Bae, Daeun Kyung, Jaehee Ryu, Eunbyeol Cho, Gyubok Lee, Sunjun Kweon, Jungwoo Oh, Lei Ji, Eric Chang, Tackeun Kim, et al. Ehrxqa: A multi-modal question answering dataset for electronic health records with chest x-ray images. *Advances in Neural Information Processing Systems*, 36, 2024.

[103] Asma Ben Abacha, Sadid A. Hasan, Vivek V. Datla, Joey Liu, Dina Demner-Fushman, and Henning Müller. Vqa-med: Overview of the medical visual question answering task at imageclef 2019. In *Working Notes of CLEF 2019*, volume 2380 of *CEUR Workshop Proceedings*, Lugano, Switzerland, September 9-12 2019. CEUR-WS.org.

[104] Xinlu Zhang, Chenxin Tian, Xianjun Yang, Lichang Chen, Zekun Li, and Linda Ruth Petzold. Alpacare:instruction-tuned large language models for medical application, 2025.

[105] Xidong Wang, Nuo Chen, Junyin Chen, Yan Hu, Yidong Wang, Xiangbo Wu, Anningzhe Gao, Xiang Wan, Haizhou Li, and Benyou Wang. Apollo: Lightweight multilingual medical llms towards democratizing medical ai to 6b people, 2024.

[106] Asma Ben Abacha and Dina Demner-Fushman. A question-entailment approach to question answering. *BMC Bioinform.*, 20(1):511:1–511:23, 2019.

[107] Di Jin, Eileen Pan, Nassim Oufattolle, Wei-Hung Weng, Hanyi Fang, and Peter Szolovits. What disease does this patient have? a large-scale open domain question answering dataset from medical exams. *Applied Sciences*, 11(14):6421, 2021.

[108] Chaoyi Wu, Weixiong Lin, Xiaoman Zhang, Ya Zhang, Yanfeng Wang, and Weidi Xie. Pmc-llama: Towards building open-source language models for medicine, 2023.

[109] Yunxiang Li, Zihan Li, Kai Zhang, Ruilong Dan, Steve Jiang, and You Zhang. Chatdoctor: A medical chat model fine-tuned on a large language model meta-ai (llama) using medical domain knowledge, 2023.

[110] Junying Chen, Xidong Wang, Anningzhe Gao, Feng Jiang, Shunian Chen, Hongbo Zhang, Dingjie Song, Wenyu Xie, Chuyi Kong, Jianquan Li, Xiang Wan, Haizhou Li, and Benyou Wang. Huatuogpt-ii, one-stage training for medical adaption of llms, 2023.

[111] Guoxin Wang, Minyu Gao, Shuai Yang, Ya Zhang, Lizhi He, Liang Huang, Hanlin Xiao, Yexuan Zhang, Wanyue Li, Lu Chen, Jintao Fei, and Xin Li. Citrus: Leveraging expert cognitive pathways in a medical language model for advanced medical decision support, 2025.

[112] Junying Chen, Zhenyang Cai, Ke Ji, Xidong Wang, Wanlong Liu, Rongsheng Wang, Jianye Hou, and Benyou Wang. Huatuogpt-o1, towards medical complex reasoning with llms, 2024.

[113] Juncheng Wu, Wenlong Deng, Xingxuan Li, Sheng Liu, Taomian Mi, Yifan Peng, Ziyang Xu, Yi Liu, Hyunjin Cho, Chang-In Choi, Yihan Cao, Hui Ren, Xiang Li, Xiaoxiao Li, and Yuyin Zhou. Medreason: Eliciting factual medical reasoning steps in llms via knowledge graphs, 2025.

[114] hw hwei. Medthoughts-8k dataset, 2025.

[115] Kenneth Marino, Mohammad Rastegari, Ali Farhadi, and Roozbeh Mottaghi. Ok-vqa: A visual question answering benchmark requiring external knowledge, 2019.

[116] Dustin Schwenk, Apoorv Khandelwal, Christopher Clark, Kenneth Marino, and Roozbeh Mottaghi. A-okvqa: A benchmark for visual question answering using world knowledge, 2022.

[117] Anand Mishra, Shashank Shekhar, Ajeet Kumar Singh, and Anirban Chakraborty. Ocr-vqa: Visual question answering by reading text in images. In *ICDAR*, 2019.

[118] Oleksii Sidorov, Ronghang Hu, Marcus Rohrbach, and Amanpreet Singh. Textcaps: a dataset for image captioningwith reading comprehension. In *European Conference on Computer Vision*, 2020.

[119] Haotian Liu, Chunyuan Li, Yuheng Li, and Yong Jae Lee. Improved baselines with visual instruction tuning, 2024.

[120] Matt Deitke, Christopher Clark, Sangho Lee, Rohun Tripathi, Yue Yang, Jae Sung Park, Mohammadreza Salehi, Niklas Muennighoff, Kyle Lo, Luca Soldaini, Jiasen Lu, Taira Anderson, Erin Bransom, Kiana Ehsani, Huong Ngo, YenSung Chen, Ajay Patel, Mark Yatskar, Chris Callison-Burch, Andrew Head, Rose Hendrix, Fayyen Bastani, Eli VanderBilt, Nathan Lambert, Yvonne Chou, Arnavi Chheda, Jenna Sparks, Sam Skjonsberg, Michael Schmitz, Aaron Sarnat, Byron Bischoff, Pete Walsh, Chris Newell, Piper Wolters, Tanmay Gupta, Kuo-Hao Zeng, Jon Borchardt, Dirk Groeneveld, Crystal Nam, Sophie Lebrecht, Caitlin Wittlif, Carissa Schoenick, Oscar Michel, Ranjay Krishna, Luca Weihs, Noah A. Smith, Hannaneh Hajishirzi, Ross Girshick, Ali Farhadi, and Aniruddha Kembhavi. Molmo and pixmo: Open weights and open data for state-of-the-art vision-language models, 2024.

[121] Teknium. Openhermes 2.5: An open dataset of synthetic data for generalist llm assistants, 2023.

[122] Guiming Hardy Chen, Shunian Chen, Ruifei Zhang, Junying Chen, Xiangbo Wu, Zhiyi Zhang, Zhihong Chen, Jianquan Li, Xiang Wan, and Benyou Wang. Allava: Harnessing gpt4v-synthesized data for a lite vision-language model, 2024.

[123] Guha Balakrishnan, Amy Zhao, Mert R Sabuncu, John Guttag, and Adrian V Dalca. Voxel-morph: A learning framework for deformable medical image registration. *IEEE Transactions on Medical Imaging*, 38(8):1788–1800, 2019.

[124] Shuai Bai, Keqin Chen, Xuejing Liu, Jialin Wang, Wenbin Ge, Sibo Song, Kai Dang, Peng Wang, Shijie Wang, Jun Tang, et al. Qwen2. 5-vl technical report. *arXiv preprint arXiv:2502.13923*, 2025.

[125] Hantian Ding, Zijian Wang, Giovanni Paolini, Varun Kumar, Anoop Deoras, Dan Roth, and Stefano Soatto. Fewer truncations improve language modeling. *arXiv preprint arXiv:2404.10830*, 2024.

[126] Yuze Zhao, Jintao Huang, Jinghan Hu, Xingjun Wang, Yunlin Mao, Daoze Zhang, Zeyinzi Jiang, Zhikai Wu, Baole Ai, Ang Wang, et al. Swift: a scalable lightweight infrastructure for fine-tuning. In *Proceedings of the AAAI Conference on Artificial Intelligence*, volume 39, pages 29733–29735, 2025.

[127] Solomon Golomb. Run-length encodings (corresp.). *IEEE transactions on information theory*, 12(3):399–401, 1966.

[128] Yuxin Zuo, Shang Qu, Yifei Li, Zhangren Chen, Xuekai Zhu, Ermo Hua, Kaiyan Zhang, Ning Ding, and Bowen Zhou. Medxpertqa: Benchmarking expert-level medical reasoning and understanding. *arXiv preprint arXiv:2501.18362*, 2025.

[129] Qiao Jin, Bhuwan Dhingra, Zhengping Liu, William W Cohen, and Xinghua Lu. Pubmedqa: A dataset for biomedical research question answering. *arXiv preprint arXiv:1909.06146*, 2019.

[130] Ankit Pal, Logesh Kumar Umapathi, and Malaikannan Sankarasubbu. Medmcqa: A large-scale multi-subject multi-choice dataset for medical domain question answering. In *Conference on health, inference, and learning*, pages 248–260. PMLR, 2022.

[131] Di Jin, Eileen Pan, Nassim Oufattolle, Wei-Hung Weng, Hanyi Fang, and Peter Szolovits. What disease does this patient have? a large-scale open domain question answering dataset from medical exams, 2020.

[132] Haonan Li, Yixuan Zhang, Fajri Koto, Yifei Yang, Hai Zhao, Yeyun Gong, Nan Duan, and Timothy Baldwin. Cmmlu: Measuring massive multitask language understanding in chinese. *arXiv preprint arXiv:2306.09212*, 2023.

[133] Hanjie Chen, Zhouxiang Fang, Yash Singla, and Mark Dredze. Benchmarking large language models on answering and explaining challenging medical questions. In *Proceedings of the 2025 Conference of the Nations of the Americas Chapter of the Association for Computational Linguistics: Human Language Technologies (Volume 1: Long Papers)*, pages 3563–3599, 2025.

[134] Xinrun Du, Yifan Yao, Kaijing Ma, Bingli Wang, Tianyu Zheng, King Zhu, Minghao Liu, Yiming Liang, Xiaolong Jin, Zhenlin Wei, et al. Supergpqa: Scaling llm evaluation across 285 graduate disciplines. *arXiv preprint arXiv:2502.14739*, 2025.

[135] Pierre Chambon, Jean-Benoit Delbrouck, Thomas Sounack, Shih-Cheng Huang, Zhihong Chen, Maya Varma, Steven QH Truong, Curtis P Langlotz, et al. Chexpert plus: Hundreds of thousands of aligned radiology texts, images and patients. *arXiv e-prints*, pages arXiv–2405, 2024.

[136] Zeki Kuş and Musa Aydin. Medsegbench: A comprehensive benchmark for medical image segmentation in diverse data modalities. *Scientific Data*, 11(1):1283, 2024.

- [137] OpenAI. Gpt-4.1: Advanced language model for multimodal and reasoning tasks. <https://openai.com/research/gpt-4-1>, 2024. Accessed: 2025-09-16. A large-scale multimodal language model with enhanced reasoning capabilities, supporting text generation, question answering, and multimodal understanding.
- [138] OpenAI. Gpt-5. <https://openai.com/gpt-5>, 2025. Accessed: 2025-09-16. A large - scale language model developed by OpenAI.
- [139] Doubao. Doubao seed 1.6. https://seed.bytedance.com/en/seed1_6, 2024. Accessed: 2025-09-16. An intelligent language model developed by Doubao, supporting tasks such as text generation, knowledge question answering, and scenario-based content creation, with optimized performance in accuracy and contextual understanding.
- [140] Andrew Sellergren, Sahar Kazemzadeh, Tiam Jaroensri, Atila Kiraly, Madeleine Traverse, Timo Kohlberger, Shawn Xu, Fayaz Jamil, Cian Hughes, Charles Lau, et al. Medgemma technical report. *arXiv preprint arXiv:2507.05201*, 2025.
- [141] Junying Chen, Chi Gui, Ruyi Ouyang, Anningzhe Gao, Shunian Chen, Guiming Hardy Chen, Xidong Wang, Ruifei Zhang, Zhenyang Cai, Ke Ji, et al. Huatuogpt-vision, towards injecting medical visual knowledge into multimodal llms at scale. *arXiv preprint arXiv:2406.19280*, 2024.
- [142] Weiwen Xu, Hou Pong Chan, Long Li, Mahani Aljunied, Ruifeng Yuan, Jianyu Wang, Chenghao Xiao, Guizhen Chen, Chaoqun Liu, Zhaodonghui Li, et al. Lingshu: A generalist foundation model for unified multimodal medical understanding and reasoning. *arXiv preprint arXiv:2506.07044*, 2025.
- [143] Tianwei Lin, Wenqiao Zhang, Sijing Li, Yuqian Yuan, Binhe Yu, Haoyuan Li, Wanggui He, Hao Jiang, Mengze Li, Xiaohui Song, et al. Healthgpt: A medical large vision-language model for unifying comprehension and generation via heterogeneous knowledge adaptation. *arXiv preprint arXiv:2502.09838*, 2025.
- [144] Chin-Yew Lin. Rouge: A package for automatic evaluation of summaries. In *Text summarization branches out*, pages 74–81, 2004.
- [145] Ramakrishna Vedantam, C Lawrence Zitnick, and Devi Parikh. Cider: Consensus-based image description evaluation. In *Proceedings of the IEEE conference on computer vision and pattern recognition*, pages 4566–4575, 2015.
- [146] Weike Zhao, Chaoyi Wu, Xiaoman Zhang, Ya Zhang, Yanfeng Wang, and Weidi Xie. Ratescore: A metric for radiology report generation. *arXiv preprint arXiv:2406.16845*, 2024.

A Case Studies



Chest X-ray

Please review the given images and generate a report that includes findings and impressions. Use this format for your response: Findings: {} Impression: {} Let's think step by step.

Step 1 – Soft tissues and bony thorax: I first use the global rib region ("Part": "rib", "bbox": "[70, 23, 869, 1004]") to survey the chest wall, clavicles, scapulae, and ribs to ensure coverage of the entire bony thorax. I then use ("Part": "right_rib", "bbox": "[75, 21, 400, 999]") and ("Part": "left_rib", "bbox": "[555, 30, 892, 999]") to focus on both sides, assessing for cortical discontinuity or lytic/osteoblastic changes—none seen. Within ("Part": "vertebrae", "bbox": "[378, 20, 598, 782]") I evaluate vertebral alignment and height; no acute compression or malalignment. The neck/axillary soft-tissue contours are symmetric, with no subcutaneous emphysema. **Step 2 – Lungs (right-left comparison):** I assess both lungs globally within ("Part": "lung", "bbox": "[90, 63, 878, 860]"). Then compare sides using ("Part": "right_lung", "bbox": "[89, 67, 455, 821]") and ("Part": "left_lung", "bbox": "[525, 65, 877, 855]"). **Increased lucency is present in the left upper lung.** Pulmonary vascular markings are normally distributed from the hilus to the periphery, without crowding or pruning-like diminution. Lobar assessment: right upper lobe ("Part": "lung_upper_lobe_right", "bbox": "[113, 390, 362, 600]"), right lower lobe ("Part": "lung_lower_lobe_right", "bbox": "[188, 330, 430, 816]"), as well as the left upper lobe ("Part": "lung_upper_lobe_left", "bbox": "[523, 65, 871, 582]") (increased lucency) and left lower lobe ("Part": "lung_lower_lobe_left", "bbox": "[532, 370, 876, 858]"). Show no focal consolidation, signs of interstitial edema, or atelectatic linear bands. No pleural line or peripheral hyperlucent area is seen to suggest pneumothorax.

Step 3 – Hila and mediastinum: I focus on the hilar regions using ("Part": "right_lung_hilum", "bbox": "[272, 66, 454, 816]") and ("Part": "left_lung_hilum", "bbox": "[522, 65, 696, 826]"). The hilae are normal in size and density, with no mass effect or lymphadenopathy. Mediastinal contours (including the aortic knob and the aortopulmonary window) are within expected limits, with no widening.

Step 4 – Diaphragm and costophrenic angles: Using the lower-lobe regions ("Part": "lung_lower_lobe_right", "bbox": "[188, 330, 430, 816]") and ("Part": "lung_lower_lobe_left", "bbox": "[532, 370, 876, 858]"). The domes are smooth and the costophrenic angles are sharp, with no blunting to suggest pleural effusion. No subdiaphragmatic free air is seen.

Step 5 – Cardiac silhouette and great vessels: Within ("Part": "heart", "bbox": "[333, 408, 655, 665]") I assess cardiac size and contours. The cardiothoracic ratio is within normal limits (<0.5); the right atrial and left ventricular borders are well defined, with no enlargement. The pulmonary vasculature is not congested.

Step 6 – Lines/tubes/devices: Survey of the entire thoracic field ("Part": "lung", "bbox": "[90, 63, 878, 860]") and soft tissues shows no endotracheal tube, central venous catheter, chest tube, or other devices. No radiopaque foreign body is identified.

Synthesis: Increased lucency in the left upper lung; otherwise both lungs are clear, with no consolidation, edema, effusion, or pneumothorax; hila and mediastinum are normal; cardiac size and pulmonary vasculature are normal; bony structures are intact.

</think>

Findings: Increased lucency in the left upper lung. The remainder of both lungs is clear, with no focal consolidation, pleural effusion, or pneumothorax. Cardiac size and pulmonary vascular markings are within normal limits. Mediastinal contours are normal. No acute osseous abnormality.

Impression: **Increased lucency in the left upper lung; correlate clinically for hereditary lobar emphysema (cannot be confirmed on a frontal chest radiograph).**





Chest X-ray

Please generate a report for the given images, including both findings and impressions. Return the report in the following format: Findings: {} Impression: {}.

Step 1 – Soft tissues and bony thorax: Using the global rib region <bbox>("Part": "rib", "bbox": "[20, 34, 899, 835]"</bbox>), I evaluated the chest wall, clavicles, scapulae, and ribs to ensure complete coverage of the thoracic cage. Then, with <bbox>("Part": "right_rib", "bbox": "[26, 37, 371, 837]"</bbox> and <bbox>("Part": "left_rib", "bbox": "[533, 47, 885, 837]"</bbox>), I focused on both sides to check for cortical discontinuity or osteolytic/osteoblastic changes—none observed. Within <bbox>("Part": "vertebrae", "bbox": "[343, 22, 574, 782]"</bbox>), vertebral alignment and heights were assessed; no acute compression or destructive lesions were seen. Cervical/axillary soft tissue contours were symmetrical, without subcutaneous emphysema.

Step 2 – Lungs (bilateral comparison): Within <bbox>("Part": "lung", "bbox": "[33, 67, 899, 820]"</bbox>), I evaluated both lungs globally, then compared right and left using <bbox>("Part": "right_lung", "bbox": "[32, 79, 799, 437]"</bbox> and <bbox>("Part": "left_lung", "bbox": "[505, 82, 899, 437]"</bbox>). I focused on both sides to check for cortical discontinuity or osteolytic/osteoblastic changes—none observed. Within <bbox>("Part": "lung", "bbox": "[33, 67, 899, 820]"</bbox>), I evaluated both lungs globally, then compared right and left using <bbox>("Part": "right_lung", "bbox": "[32, 79, 799, 437]"</bbox> and <bbox>("Part": "left_lung", "bbox": "[505, 82, 899, 437]"</bbox>). Diffuse lung hyperinflation was noted, with increased lucency. Vascular markings appeared reduced toward the periphery. Segmental assessment: right upper lobe <bbox>("Part": "lung_upper_lobe_right", "bbox": "[100, 80, 421, 437]"</bbox>), right middle lobe <bbox>("Part": "lung_middle_lobe_right", "bbox": "[432, 79, 799, 437]"</bbox>), right lower lobe <bbox>("Part": "lung_lower_lobe_right", "bbox": "[505, 80, 899, 437]"</bbox>), left upper lobe <bbox>("Part": "lung_upper_lobe_left", "bbox": "[505, 82, 899, 437]"</bbox>), left middle lobe <bbox>("Part": "lung_middle_lobe_left", "bbox": "[505, 82, 899, 437]"</bbox>), and left lower lobe <bbox>("Part": "lung_lower_lobe_left", "bbox": "[517, 80, 899, 437]"</bbox>)—no focal consolidation, interstitial edema, nodules, or atelectatic strands identified. No pleural line or lucent area suggestive of pneumothorax.

Step 3 – Hila and mediastinum: Using <bbox>("Part": "right_lung_hilum", "bbox": "[238, 79, 454, 437]"</bbox> and <bbox>("Part": "left_lung_hilum", "bbox": "[522, 79, 899, 437]"</bbox>), I focused on the hilar regions. **Bilateral hilar shadows are enlarged, and pulmonary arteries are thickened and widened. The mediastinal contour (including aortic arch and main pulmonary artery window) showed no significant widening.**

Step 4 – Diaphragm and costophrenic angles: Within lower lung fields <bbox>("Part": "lung_lower_lobe_right", "bbox": "[31, 820, 454, 864]"</bbox> and <bbox>("Part": "lung_lower_lobe_left", "bbox": "[517, 820, 899, 864]"</bbox>), both diaphragms appeared flattened and depressed. Costophrenic angles were sharp, with no blunting suggestive of pleural effusion. No subdiaphragmatic free air observed.

Step 5 – Cardiac silhouette and great vessels: Within <bbox>("Part": "heart", "bbox": "[336, 408, 656, 665]"</bbox>), I assessed cardiac size and contour. Cardiothoracic ratio was clearly <0.5; right atrial and left ventricular borders were distinct, with no enlargement.

Step 6 – Foreign bodies/devices: A survey of the entire thoracic field <bbox>("Part": "lung", "bbox": "[33, 67, 899, 820]"</bbox>), and surrounding soft tissues revealed no endotracheal tube, central venous catheter, chest drain, or other devices. No radiopaque foreign bodies were identified.

</think>

Findings: Diffuse lung hyperinflation with increased lucency. No focal consolidation, pleural effusion, or pneumothorax. Pulmonary arteries are thickened and widened, with bilateral hilar enlargement. Both diaphragms are flattened. Cardiac silhouette within normal limits. No acute bony abnormalities.

Impression: **Imaging findings are consistent with chronic obstructive pulmonary disease (COPD) with associated pulmonary hypertension.**



38

Chest X-ray



请审查给定的图像并创建一份概述检查结果和诊断意见的报告。请使用以下格式进行报告：检查结果：{} 诊断意见：{}。请逐步思考分析。

<think>

步骤1 - 软组织与骨性胸廓：我首先沿胸壁外侧及软组织追踪，未见皮下气肿或软组织异常。随后使用 `<bbox>["Part": "rib", "bbox": "[69, 0, 872, 893]"</bbox>` 评估肋骨，并分别用 `<bbox>["Part": "right_rib", "bbox": "[84, 0, 450, 893]"</bbox>` 和 `<bbox>["Part": "left_rib", "bbox": "[518, 0, 888, 893]"</bbox>` 评估两侧。在这些框内可见肋骨完整，无移位性骨折；锁骨与肩胛骨轮廓对称。于 `<bbox>["Part": "vertebrae", "bbox": "[468, 0, 898, 893]"</bbox>` 范围内复查脊柱，排列保持良好，未见急性压缩性畸形。

步骤2 - 肺（左右对比）：我使用 `<bbox>["Part": "lung", "bbox": "[113, 22, 860, 650]"</bbox>` 评估整体肺野，然后分别用 `<bbox>["Part": "right_lung", "bbox": "[115, 23, 480, 650]"</bbox>` 和 `<bbox>["Part": "left_lung", "bbox": "[482, 23, 850, 650]"</bbox>` 评估两侧。上肺区（`<bbox>["Part": "lung_upper_lobe", "bbox": "[175, 23, 445, 285]"</bbox>` 和 `<bbox>["Part": "lung_upper_lobe_right", "bbox": "[175, 23, 445, 285]"</bbox>`）通气清晰，血管纹理正常。中下肺区（`<bbox>["Part": "lung_middle_lobe_right", "bbox": "[175, 23, 445, 285]"</bbox>` 和 `<bbox>["Part": "lung_lower_lobe_right", "bbox": "[175, 23, 445, 285]"</bbox>`）**可见双侧斑片状、边界不清的致密影**，以基底部最为明显，考虑肺泡性病变。未见局灶性空洞形成或肿块样致密影。未见提示气胸的胸膜线或深沟征。

步骤3 - 肺门与纵隔：在 `<bbox>["Part": "right_lung_hilum", "bbox": "[299, 23, 669, 285]"</bbox>` 和 `<bbox>["Part": "left_lung_hilum", "bbox": "[518, 23, 888, 285]"</bbox>` 范围内，肺门结构不增大，密度正常。纵隔轮廓及主动脉弓结在AP半坐位片上均在预期范围内。

步骤4 - 肋膈角与肋膈角：双侧胸顶光滑，肋膈角锐利。未见单纯性胸腔积液。未见膈下游离气体。

步骤5 - 心影与大血管：使用 `<bbox>["Part": "heart", "bbox": "[338, 23, 708, 285]"</bbox>` 评估，心影大小在AP半坐位技术条件下属正常范围。心胸比未增大。心脏轮廓保留良好。

步骤6 - 异物/器械：气管插管沿气管中央行走，**管尖位于隆突上方数厘米——位置合适**。易胃管下降越过膈肌进入胃内。右侧颈内静脉中心静脉导管向内侧行走，管尖投影于上腔静脉中段区域。胸前可见多枚心电图电极与导线。未见胸腔引流管或其他装置。

</think>

<answer>

检查结果
双侧肺下叶可见斑片状、边界不清的斑片状致密影
未见气胸或胸腔积液
气管插管
鼻胃管及中心静脉导管位置恰当

诊断意见
考虑肺水肿，亦需鉴别感染性肺炎



</answer>

Chest X-ray



这是一张AP位胸部X光，请逐步思考分析这张影像，并生成一份包含findings和impression的报告。

<think>

步骤1 - 软组织与骨性胸廓：我首先使用全局肋骨区域 `<bbox>["Part": "rib", "bbox": "[120, 0, 875, 893]"</bbox>` 扫描胸壁、锁骨、肩胛骨及肋骨，以确保覆盖整个骨性胸廓。随后分别使用 `<bbox>["Part": "right_rib", "bbox": "[136, 0, 506, 893]"</bbox>` 和 `<bbox>["Part": "left_rib", "bbox": "[518, 0, 888, 893]"</bbox>` 聚焦两侧，检查皮质连续性中断或骨/成骨性改变——未见。于 `<bbox>["Part": "vertebrae", "bbox": "[518, 0, 888, 893]"</bbox>` 范围内评估椎体排列与高度，未见急性压缩或错位。锁骨/腋窝软组织轮廓对称。未见皮下气肿。

步骤2 - 肺（左右对比）：我在 `<bbox>["Part": "lung", "bbox": "[113, 22, 860, 650]"</bbox>` 范围内整体评估双肺，然后使用 `<bbox>["Part": "right_lung", "bbox": "[115, 23, 480, 650]"</bbox>` 和 `<bbox>["Part": "left_lung", "bbox": "[482, 23, 850, 650]"</bbox>` 进行两侧比较。右下叶 `<bbox>["Part": "lung_lower_lobe_right", "bbox": "[115, 23, 480, 650]"</bbox>` **显示变密度**，**左下叶肋膈角** `<bbox>["Part": "lung_lower_lobe_left", "bbox": "[482, 23, 850, 650]"</bbox>` **显示深沟征**。右侧肋膈角显示深沟征，**左侧肋膈角** `<bbox>["Part": "lung_lower_lobe_left", "bbox": "[482, 23, 850, 650]"</bbox>` **显示钝化**，提示胸腔积液。其余肺野未见局灶性实变或明显结节影。

步骤3 - 肺门与纵隔：我使用 `<bbox>["Part": "right_lung_hilum", "bbox": "[310, 23, 680, 650]"</bbox>` 和 `<bbox>["Part": "left_lung_hilum", "bbox": "[518, 23, 888, 650]"</bbox>` 重点观察肺门区。肺门大小与密度正常，无占位反应或淋巴结肿大。纵隔轮廓（包括主动脉弓结与主肺动脉窗）在预期范围内，无增宽。

步骤4 - 利用下叶区域：`<bbox>["Part": "lung_lower_lobe_right", "bbox": "[115, 23, 480, 650]"</bbox>` 和 `<bbox>["Part": "lung_lower_lobe_left", "bbox": "[482, 23, 850, 650]"</bbox>` 评估。右侧肋膈角显示深沟征，**左侧肋膈角钝化**，提示少量胸腔积液。心影大小正常，未见急性骨性异常。

步骤5 - 心影与大血管：我在 `<bbox>["Part": "heart", "bbox": "[338, 23, 708, 650]"</bbox>` 范围内评估心脏大小与轮廓。心胸比在正常范围内(<0.5)。心影轮廓尚清，肺血管未充血。

步骤6 - 异物/器械：扫描整个胸部视野 `<bbox>["Part": "lung", "bbox": "[113, 22, 860, 650]"</bbox>` 及软组织，可见右侧PICC导管末端位于心包前上腔静脉内；右侧胸腔引流管在位。未见其他管道或异物。

综合：右下叶受压性不张；右侧深沟征提示气胸；左侧肋膈角钝化提示少量胸腔积液。心影及纵隔形态基本正常。骨性结构完整。

</think>

<answer>

检查所见：右侧PICC管末端位于心包前上腔静脉，右侧胸腔引流管在位。右下叶受压性不张，右侧肋膈角深沟征提示气胸，左侧肋膈角钝化，提示胸腔积液。心影大小正常。未见急性骨性异常。

诊断意见：右侧气胸并右下叶受压性不张；左侧胸腔积液。



</answer>

Chest X-ray


请分析下这个X光影像。请逐步思考分析。并生成一份包含检查所见和诊断意见的报告。

<think>

步骤1—软组织与骨性胸廓：我首先使用全局肋骨区域 `<bbox>["Part":"rib",
"bbox": "[70, 23, 845, 996]"</bbox>` 扫描胸壁、锁骨、肩胛骨及肋骨，以确保覆盖整个骨性胸廓。随后分别使用 `<bbox>["Part":"right rib",
"bbox": "[70, 23, 396, 996]"</bbox>` 和 `<bbox>["Part":"left rib",
"bbox": "[527, 23, 845, 996]"</bbox>` 聚焦两侧，检查皮质连续性中断或溶骨/成骨性改变——未见。于 `<bbox>["Part":"vertebrae",
"bbox": "[330, 30, 530, 773]"</bbox>` 范围内评估椎体排列与高度，未见急性压缩或错位。颈部/锁窝软组织轮廓正常，未见皮下气肿。

步骤2—肺（左右对比）：我在 `<bbox>["Part":"lung",
"bbox": "[89, 57, 845, 400]"</bbox>` 范围内整体评估双肺，然后使用 `<bbox>["Part":"right lung",
"bbox": "[87, 65, 421, 781]"</bbox>` 和 `<bbox>["Part":"left lung",
"bbox": "[490, 60, 845, 781]"</bbox>` 进行两侧比较。左肺透亮度普遍增加，伴容积增大及膈下降，肺纹理减少。右下叶 `<bbox>["Part":"lung lower lobe right",
"bbox": "[87, 370, 421, 422]"</bbox>` 可见片状混浊影，并存有轻度支气管充气征。右上叶 `<bbox>["Part":"lung upper lobe right",
"bbox": "[87, 400, 421, 422]"</bbox>` 与右中叶 `<bbox>["Part":"lung middle lobe right",
"bbox": "[106, 393, 421, 422]"</bbox>` 未见异常。左上叶 `<bbox>["Part":"lung upper lobe left",
"bbox": "[490, 393, 845, 422]"</bbox>` 与左下叶 `<bbox>["Part":"lung lower lobe left",
"bbox": "[513, 408, 845, 422]"</bbox>` 未见局灶性实变或条索影，未见提示气胸的肺膜线或索条征。

步骤3—肺门与纵隔：我使用 `<bbox>["Part":"right lung hilum",
"bbox": "[251, 65, 421, 781]"</bbox>` 和 `<bbox>["Part":"left lung hilum",
"bbox": "[489, 65, 845, 781]"</bbox>` 重点观察肺门区。肺门大小与密度正常，无占位反应或淋巴结肿大。纵隔轮廓（包括主动脉弓与主肺动脉窗）在预期范围内，无增宽。

步骤4—膈肌与肋膈角：利用下叶区域 `<bbox>["Part":"lung lower lobe right",
"bbox": "[87, 370, 421, 422]"</bbox>` 和 `<bbox>["Part":"lung lower lobe left",
"bbox": "[513, 408, 845, 422]"</bbox>`，可见左侧膈下降，右侧膈顶光滑。双侧肋膈角锐利，未见钝化或提示胸腔积液。未见游离气体。

步骤5—心脏与大血管：我在 `<bbox>["Part":"heart",
"bbox": "[305, 413, 845, 422]"</bbox>` 范围内评估心脏大小与轮廓。心胸比在正常范围内 (<0.5)，右心房与左心室边界清晰，无增大。肺血管未见充血。

步骤6—异物/器械：扫描整个胸部视野 `<bbox>["Part":"lung",
"bbox": "[89, 57, 845, 400]"</bbox>` 及软组织，未见气管插管、中心静脉导管、胸腔引流管或其他装置。未见放射不透性异物。

</think>

<answer>

检查所见：左肺透亮度增加，容积增大，膈下降，肺纹理减少。右肺下叶见片状混浊影，存在**轻度支气管充气征**。心影大小及纵隔结构正常。双侧肋膈角锐利。骨性胸廓完整。

诊断意见：右肺下叶肺炎表现；**左肺代偿性改变**。

</answer>



Blood Test Report


请将图中检验单表格解析为 Markdown 格式，表头包括检验项目、结果、单位、参考范围

检验项目|结果|单位|参考区间|检验项目|结果|单位|参考区间|

WBC|4.2|10⁹/L|3.50--9.50|平均红细胞体积 MCV|82.5|fL|82.0--100.0|
 淋巴细胞% LYMPH|44.5%|2.0--50.0|平均血红蛋白浓度 MCH|29.8|pg|27.0--34.0|
 单核细胞% MONO%|7.5%|3.0--10.0|平均血红蛋白浓度 MCHC|34.5|g/L|316--354|
 中性粒细胞% NEUT%|40.6%|40.0--75.0|红细胞体积宽度 RDW|12.4%|11.5--15.5|
 嗜酸性细胞% EOS%|6.7%|0--8.0|血小板计数 PLT|211|10⁹/L|125--350|
 嗜碱性细胞% BAS%|0.7%|0.0--1.0|平均血小板体积 MPV|10.0|fL|6.8--13.5|
 淋巴细胞绝对值 LYMPH|3.73|10⁹/L|1.10--3.20|血小板比容 PCT|0.21|0.00--0.99|
 单核细胞绝对值 MONO#|0.63|10⁹/L|0.10--0.60|平均血小板体积 PDW|11.0|fL|9.8--17.0|
 中性粒细胞绝对值 NEU#|3.42|10⁹/L|1.80--6.30|C-反应蛋白 CRP|8.69|mg/L|0.00--8.00|
 嗜酸性细胞绝对值 EOS#|0.56|10⁹/L|0.02--1.5|血浆淀粉样蛋白 A SAA|10.45|mg/L|0.00--10.00|
 嗜碱性细胞绝对值 BAS#|0.06|10⁹/L|0.00--0.06|
 红细胞计数 RBC|4.66|10¹²/L|4.450--5.80|
 血红蛋白 HGB|139|g/L|130--175|
 红细胞压积 HCT|40.3|0.400--0.500|



Medication Packages


请输入图中包含的药品名称，如果有贴纸上的用法用量也请输出

药品名称|用法用量|

磷酸奥司他韦干混悬剂|未显示|
 盐酸西替利嗪口服溶液|一天2次，一次2.5ml|
 盐酸氨溴索口服溶液|一天3次，一次2.5ml|
 金振口服液|一天2次，一次1支|







Chest X-ray



What is the specific abnormality present in this image? Please solve this step-by-step.



A large mass is present in the left hemithorax, obscuring the left hilum and occupying most of the upper lung field. The right lung appears clear, and the cardiac and diaphragmatic contours are preserved.



Brain CT



What is abnormal in this image?



An acute intraparenchymal hemorrhage is seen in the right basal ganglia region, appearing as a hyperdense focus within the brain parenchyma. There is mild displacement of adjacent structures, including the lateral ventricle. Surrounding hypodense change is noted, which may represent edema.



Abdominal CT



Is this a CT scan of a healthy person?



No, the image does not depict a CT scan of a healthy person. The presence of **multiple hypodense lesions in the liver** is indicative of pathological changes, which could be due to various conditions such as metastatic disease, primary liver tumors, or other hepatic pathologies. These findings suggest that the patient has an underlying liver condition that requires further clinical evaluation and management.



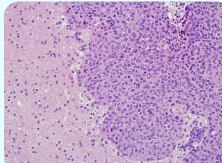
Knee Joint MRI



What can you see in this image?



A longitudinal hyperintense signal is seen within the medial meniscus with displacement of a fragment into the intercondylar notch, suggesting a bucket-handle tear. A "double PCL sign" is present in the intercondylar notch. A small joint effusion is noted. The ACL graft appears intact where visualized.



H&E-stained pathological section



What does this image show, and what did you find in it?



This image shows a histological section stained with hematoxylin and eosin (H&E). H&E-stained sections show **malignant tumor tissue**, with tumor cells displaying variable morphology. Some nuclei are markedly enlarged and hyperchromatic, and numerous mitotic figures are observed, indicating high proliferative activity of the tumor.



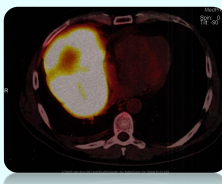
Clinical Pictures



What is abnormal in this image?



The image shows the palms of both hands with numerous symmetrically distributed, reddish-brown papules scattered across the skin. The papules are relatively uniform in size, firm, and slightly raised without obvious pustules or scaling. They are diffusely present across the palmar surfaces, with no significant underlying skin abnormalities. This appearance is characteristic of the palmar rash commonly seen in secondary syphilis.



Chest PET/CT



What are your findings?



The most prominent feature is a **large, hypermetabolic mass** occupying the right hemithorax. On PET-CT, the lesion demonstrates intense FDG uptake, consistent with a malignant process. While the pattern of involvement could mimic **malignant pleural mesothelioma**, the differential diagnosis should also include anterior mediastinal tumors such as **thymic carcinoma** or **thymic neuroendocrine carcinoma**, **lymphoma**, or other **pleural-based malignancies**. Definitive diagnosis requires histopathological confirmation.

Skin Pictures

一名 68 岁男性，3 天前出现左侧胸背部烧灼样疼痛与触痛，前日起在疼痛区出现皮疹，如图所示。体温 37.4°C。既往史：2 型糖尿病，血糖控制一般。近期因慢性腰痛自行短期口服布洛芬。患者无腋下淋巴结明显肿大，肺心音未见异常。下一步？

AI

Head CT

一名 23 岁女性，既往转移性肺腺癌住院治疗。入院时曾 >1 小时无反应，现入院第 2 天较入院时更嗜睡。气管插管状态，可自发睁眼，右上肢可间断遵嘱做简单动作。四肢对痛刺激均有回缩反应。GCS 11 (E4 V1 M6)。肌张力与肌容积正常。腱反射右侧较左侧亢进，右踝有 3 次阵挛，双侧 Babinski 征阳性。颅脑 MRI 提示患者右侧中动脉区或脑梗。参考患者后续的 CT 影像图片，最合理的下一步是？

AI

Chest X-ray

一名 20 岁男性，咳嗽与发热 2 天。既往健康。查体不中毒貌，血氧饱和度正常，右上肺区可闻及局限性湿啰音。影像如图所示。最合理的下一步是？

根据患者提供的信息和 CT 影像，患者出现了右侧中动脉区域的脑梗塞。这种情况下，患者的神经功能可能会进一步恶化，因为脑梗塞可能导致脑组织缺血和坏死。在这种情况下，最合理的下一步可能是进行手术干预。手术可能包括去骨瓣减压术或血管内治疗，以减轻颅内压力并恢复脑血流。然而，具体的治疗方案应由神经外科医生根据患者的具体情况来决定。此外，患者需要密切监测其神经功能和生命体征，以及可能的并发症，如脑水肿、脑疝等。同时，也需要继续给予支持性治疗，如维持血压稳定、控制血糖、防止感染等。总的来说，这是一个复杂的情况，需要多学科团队的合作，包括神经外科、重症医学科、康复医学科等，以提供最佳的治疗和护理。

AI

Skin Pictures

请你用中文回答这个问题：一名 57 岁男性，过去 4 周逐渐出现右下肢无力和步态不稳，近期急性加重。查体示右下肢弥漫性无力，四肢肌张力增高（右侧大于左侧），右侧踝阵挛可持续 7-8 次，步态轻度共济失调。此外，髓实质正常，但在 C3-C4 水平可见髓明显变细。患者的脊柱 MRI 如图所示。最合理的下一步是？

根据您提供的信息，患者为 57 岁男性，近 4 周出现右下肢无力和步态不稳，并且在最近几周症状有所加重。体检显示右下肢弥漫性无力，四肢肌张力增高（右侧大于左侧），右侧踝阵挛可持续 7-8 次，步态轻度共济失调。此外，髓实质正常，但在 C3-C4 水平可见髓明显变细。这些临床表现提示患者可能存在颈椎病变，特别是 C3-C4 水平的脊髓受压。MRI 图像显示该区域脊髓变细，进一步支持这一诊断。对于这种情况，最合理的下一步是进行颈椎手术治疗。手术的目标是减轻对脊髓的压力，恢复神经功能。手术方式可能包括椎板切除术、椎间盘切除术或融合术等。具体取决于病情的严重程度和患者的整体状况。然而，最终的决定应由医生根据详细的病史、体检结果和影像学检查来做出。我建议您尽快就医，以便得到适当的评估和治疗。

AI

42